Chapter 4

Photoionization cross sections in the ion yield

Due to its simplicity, the three-body system helium, in its doubly excited states, has become a highly exciting atom for the study of quantum chaos. Quantum chaos can be considered as the behavior of a quantum system whose classical counterpart behaves chaotic. Doubly excited helium approaches the semiclassical limit, i.e. $\hbar \to 0$, in the region close to the double-ionization threshold (for details see App. A). The classical counterpart of the helium atom, the classical three-body system, is a nonintegrable system, i.e. it can behave chaotic. Therefore, one expects quantum chaos to emerge in the spectra of doubly excited resonances in He close to the double-ionization threshold. In other words, close to double-ionization threshold, the signatures of classical mechanics in doubly excited helium will be magnified by the observation of quantum-chaotic spectra. Richter *et al.* [28] showed that classical helium exhibits a mixed phase space with regular and chaotic regions by using the Poincaré section of the Wannier ridge (explained later). Chaotic dynamic in classical helium is independent of the total energy. However, the spectra in doubly excited helium carry a transition (reflecting strong electron correlations) to chaotic behavior while the photon energy is increased close to the double-ionization threshold. The strong electron correlations in this two-electron atom are reflected in a set of new approximate quantum numbers $N, K_{n'}$ instead of traditional quantum numbers like l. These approximate quantum numbers work quite well, particularly in the low energy region. In the region of high doubly excited states, an increasing number of perturbers render the spectra very complicated and fluctuating. As a consequence, the approximate quantum numbers $N, K_{n'}$ start to dissolve. At the double-ionization threshold, the helium atom may be described by classical mechanics. From this point of view, one can assume that there might not be enough good quantum numbers to describe the spectra close to double-ionization threshold of helium. In the previous work of our group [18], statistical studies of nearest-neighbor spacings (NNS) of energy levels carried out, with the results that the onset of a transition to quantum chaos in the region below the SIT I_9 could be identified. From the studies presented in this dissertation, we shall see that the transition region from integrability to full chaos in

$^1P^o$ helium is much larger, in agreement with the recent findings for $^1S^e$ doubly excited helium [19].

So far, most measurements of TCSs of doubly excited resonances in helium were limited to the energy region below the SIT I_9 [18, 30, 62]. Many advanced theoretical methods [29, 31, 32, 33, 63] have been developed during last 20 years. However, these theoretical studies were performed only in the region below the SIT I_9 as well. In this chapter, we shall present our recent experimental progress on the TCS up to the SIT I_{15}. It is worthwhile to mention here that very recently state-of-the-art complex-rotation calculations for the TCS in three-dimensional helium by our cooperation partner D. Delande (Universite Pierre et Marie Curie, Paris) have reached the SIT I_{17} [27]; they are confirmed very well up to I_{15} by the present measurements. In this part, we shall first discuss the approximate quantum numbers $N, K_{n'}$ by using theoretical results and then study statistical properties of the energy levels, Fano parameters q, and linewidths of the resonances in doubly excited helium. Preliminary statistical studies for this atom displayed interesting precursor quantum signatures of chaos. Note that detailed statistical studies have to be performed predominantly with theoretical data due to the extremely low intensities of most of the Rydberg series, which give rise to the situation that only a small fraction of the doubly excited states can be observed experimentally.

4.1 Wigner distribution and Poisson distribution for energy levels

There are two different types of motion in classical mechanics: the regular motion of integrable systems and the chaotic motion of non-integrable systems. To distinguish these two motions, one may have a look at a bundle of trajectories in the phase space originating from a very narrow cloud of starting points. In the chaotic case, the distances between any of two trajectories in phase space increase exponentially in time. For a regular motion, these distances may grow in a power of time, but never exponentially. A simple example for classical integrable system, given in Fig. 4.1, is given by a one-dimensional accelerated motion with constant accelerations. X and P_X represent the spatial coordinate and the corresponding momentum of a particle, respectively. Using different values of acceleration for the calculation of the two trajectories, the distances, $d(t_i)$, between two trajectories in phase space increase in t^2, as can be seen in Fig. 4.1. In contrast, the distances between two trajectories grow linearly or remain constant in time if one varies the initial velocities or the initial positions of the trajectories, respectively. There are no possibilities to change the initial conditions so that one obtains an exponential increase of $d(t_i)$ in this integrable case. Therefore, the "exponential sensitivity" is the typical character for a classical chaotic behavior. When turning to quantum mechanics, the classical description of the exponential sensitivity to the initial conditions cannot be used any more to characterize quantum chaos. One reason is that one cannot directly observe quantum chaos in phase space due to the uncertainty principle in quantum me-

chanics. However, this results in one possibility to study quantum chaos in the phase space of its classical counterpart. A second reason is given by the fact that the wave function $\Psi(t)$ in Schrödinger's wave equation can always be calculated uniquely, and it is of a simple periodic form in t, i.e. $\Psi = \Psi_0 exp(\frac{-i}{\hbar}Et)$. This means that the exponential sensitivity in time is "suppressed" in the wave function of a quantum chaotic system. Nevertheless, most researchers agree that the deterministic features of quantum chaos should be manifested in some ways in the quantum observables such as the energy levels, line widths, and Fano parameters q of resonances in doubly excited helium.
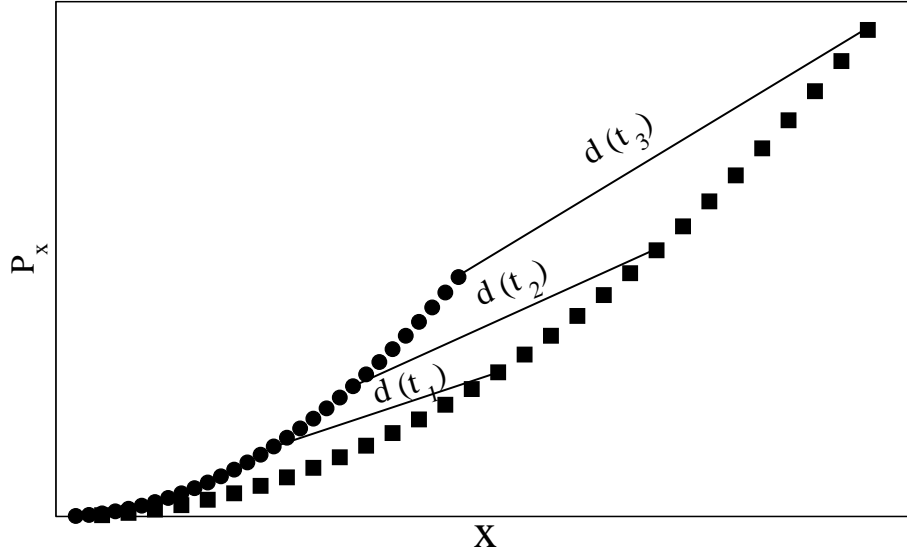

Figure 4.1: Phase space for one-dimensional accelerated motions with constant accelerations. Two trajectories that are obtained using different values of acceleration are plotted by filled circles and filled squares. The solid lines represent the distances between these two trajectories at three different times.

This raises the question how quantum chaos is manifested in the spectra. One typical manifestation is the spacing of energy levels, which will be discussed in the following. According to Heisenberg, the operators of quantum mechanics can be represented by matrices. It is then natural to conjecture that the observables of a chaotic quantum system should be represented by random matrices, i.e. the energy levels in a chaotic quantum system can be described as random elements of matrices. Some conditions based on very basic principles of physics are assumed for matrices, like the invariance of the probability density for the Hamiltonian under orthogonal transformation. Besides that the matrix elements described by the Hamiltonian must be uncorrelated. According to the invariance and the uncorrelation of the Hamiltonian, the probabilities of Hamiltonian elements are of Gaussian form, and the statistical properties of the nearest-neighbor spacings S (NNS) of energy levels are given by the Wigner distribution

$$P_W(S) = \frac{\pi}{2}S\,exp(-\frac{\pi}{4}S^2). \tag{4.1}$$

The derivation of the Wigner distribution, given in Eq. (4.1), on the basis of random matrix theory [64, 65] is described in App. B; this theory was developed in the nineteen
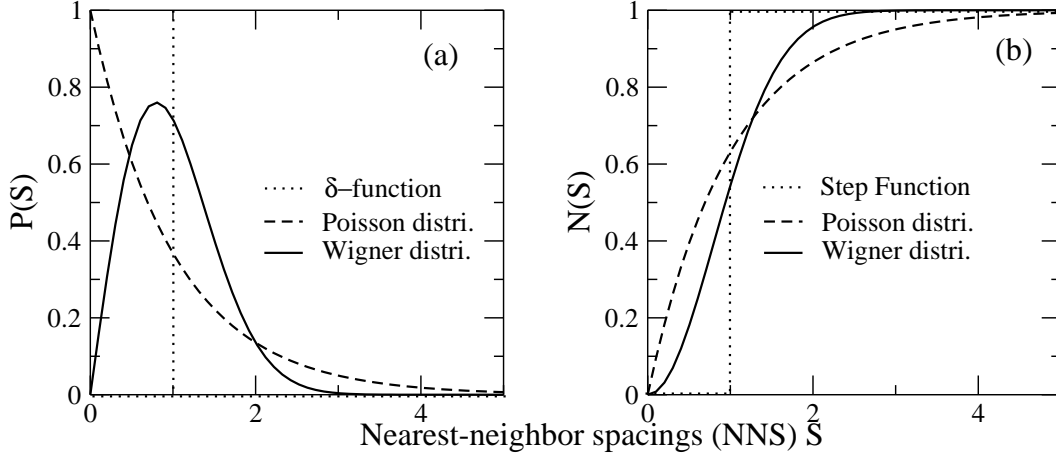
Figure 4.2: Probabilities P(S) (a) and integrated probabilities N(S) (b) as a function of the nearest-neighbor spacings (NNS) S. Solid lines and dashed lines represent Wigner distribution and Poisson distribution, respectively. Dotted lines in (a) and (b) represent a δ-function and a step function, respectively.

fifties and sixties in order to understand the distribution of energy levels in nuclei. Note that the spacings S are calculated from effective quantum numbers, which are obtained from the resonant energies E_r with the formula

$$\mu_N(E) = \sqrt{\frac{\mathcal{R}}{I_N - E_r}} \quad , \tag{4.2}$$

where $\mathcal{R}$ is the Rydberg constant. A level density in the scaled spectra is independent of photon energy.

In the spectra of an integrable system, the most probable spacing between resonances that belong to different independent Rydberg series can be zero, since these energy levels are uncorrelated. The probability distribution of the NNSs for this case is predicted to be a Poisson distribution

$$P_P(S) = exp(-S) \tag{4.3}$$

and the energy levels exhibit a level clustering, i.e. $P_P(S)$ has its maximum at $S = 0$. This is because the energy levels from various independent subsystems are decoupled from each other. In contrast to the level clustering of a Poisson distribution, the energy levels in a Wigner distribution exhibit a level repulsion

$$P_W(S \to 0) \sim S, \tag{4.4}$$

as derived from Eq. 4.1. The maximum probability in Wigner distribution appears for a mean value of S, not at $S \to 0$.

In the present case, we analyzed the statistical properties of the NNSs in helium based on the theoretical results. Since the number of resonances is limited, we used integrated Wigner or Poisson distribution for the NNSs in order to reduce statistical fluctuations. In this way we obtain

$$N_W(S) = 1 - exp(-\frac{\pi}{4}S^2) \tag{4.5}$$

and

$$N_P(S) = 1 - exp(-S) \tag{4.6}$$

for a Wigner and a Poisson distributions, respectively, with $N(S) = \int_0^S dS' P(S')$.

The Wigner and Poisson distributions given by Eqs. (4.1) and (4.3) as well as their integrated forms given by Eqs. (4.5) and (4.6) are plotted in Fig. 4.2. In order to better understand the NNS distributions, we additionally added the NNS distribution for one regular Rydberg series presented by a dotted line in this figure. In classical integrable systems, the number of constants of motion is equal to the degrees of freedom. A system with fewer constants of motion than degrees of freedom becomes non-integrable and has regions in phase space, where the dynamics is chaotic. In a transition from a classical to a quantum system, the constants of motion become quantum numbers. Therefore, one could study the chaotic dynamics by the quantum numbers of the system. In Fig. 4.2, three curves, δ-function or step function, Poisson distribution, and Wigner distribution, correspond to three different systems taking their quantum numbers into account. δ-function or step function indicate that the resonances belong to one regular Rydberg series. The reason is that quantum defect numbers should be equal for all resonances in a regular Rydberg series, which results in the unity of the NNSs [25] according to the Rydberg formula. Poisson distribution demonstrates the character of several independent subsystems. These subsystems can be regular Rydberg series or chaotic subsystems [10]. In this case, one can assume that there are still some good quantum numbers, which allow to identify separately the independent subsystems, and the corresponding system is not fully chaotic. In contrast to the δ-function and Poisson distribution, the Wigner distribution describes a chaotic system without good quantum numbers.

The Wigner distribution of NNS is a typical and universal characteristics of energy level fluctuations of chaotic quantum spectra, which is called BGS conjecture by Bohigas, Giannoni, and Schmit [66]. So far, Wigner distributions for the NNSs were observed in a variety of very different chaotic systems, ranging from atom to microwave billiard. Fig. 4.3 presents a collection of NNS distributions that result from a number of very different systems, e.g. the NNS distributions for the Sinai billiard[1] [66], the hydrogen atom in a strong magnetic field [67], for the excitation spectrum of a NO_2 molecule [68], for the acoustic resonance spectrum of a Sinai-shaped quartz block [69], for the microwave spectrum of a three-dimensional chaotic cavity [70], and for the vibration spectrum of a quarter-stadium shaped plate [71]. For all these examples including quantum and classical cases, excellent agreement with a Wigner distribution is found. Obviously, the BGS conjecture is independent of the quantum mechanical systems, but remains valid in a much more general context. Therefore, the search for a Wigner distribution of energy levels has become a standard tool to study the manifestation of chaos, i.e. many researchers regard it as a fundamental signature of quantum chaos [9].

Throughout this part of the dissertation, the Wigner distribution, the Poisson distribution, and the step function will be employed to study the dynamics of doubly excited

---

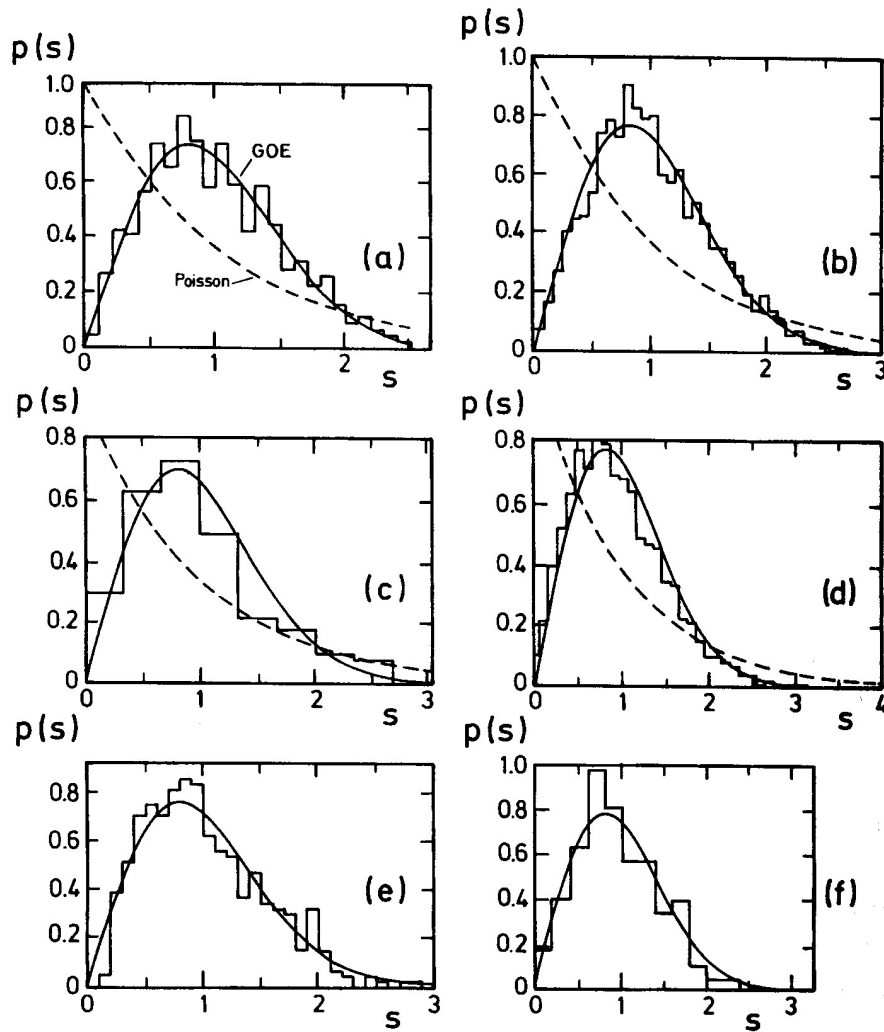[1]The billiard with a reflecting disk located in the center.

Figure 4.3: Level spacing distributions for (a) a Sinai billiard [66], (b) a hydrogen atom in a strong magnetic field [67], (c) the excitation spectrum of a NO_2 molecule [68], (d) the acoustic resonance spectrum of a Sinai-shaped quartz block [69],(e) the microwave spectrum of a three-dimensional chaotic cavity [70], and (f) the vibration spectrum of a quarter-stadium shaped plate [71]; (from Stöckmann [9])

resonances in helium in the region close to the double-ionization threshold, where quantum chaos is expected, to occur.

4.2 Ericson fluctuations and autocorrelation function

As discussed in the previous section, the Wigner distribution of the NNSs of the resonances is considered to be a standard characteristic for chaotic quantum spectra. As an additional characteristic of quantum chaos, the concept of Ericson fluctuations was developed by Ericson in 1960 [26]; it was originally related to investigations of fluctuat-

ing nuclear spectra. Nowadays, these Ericson fluctuations are considered to be a general fingerprint for quantum chaotic scattering rather than only a nuclear phenomenon [10].
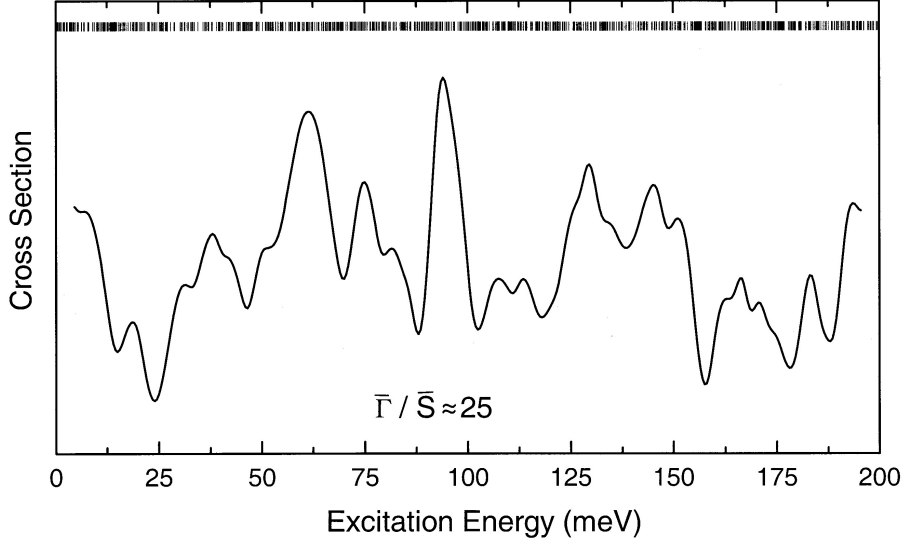

Figure 4.4: Simulated spectrum of Ericson fluctuations characterized by $\Lambda = \bar{\Gamma}/\bar{S} \gg 1$. The spectrum convoluted with a Gaussian function of 1.5 meV (FWHM) is plotted as a function of relative excitation energy. The energy positions of resonances are indicated by the vertical bars.

The Ericson fluctuations can be observed if the resonances in the spectra are strongly overlapping and the intensities of these resonances are randomly distributed, i.e. can be considered to be of the same order of magnitude. The strong overlap means that the average decay width, $\bar{\Gamma}$, of the resonances is much larger than their average energy spacing, $\bar{S}$. This can be quantified by defining the Ericson parameter, $\Lambda = \bar{\Gamma}/\bar{S}$. The above described case of $\Lambda = \bar{\Gamma}/\bar{S} \gg 1$ is defined as Eriscon regime. If these two prerequisites, $\Lambda \gg 1$ and a comparable intensity of all resonances, are fulfilled, a spectrum consists of fluctuations which cannot be identified with single resonances. These Ericson fluctuations can be observed in a simulated spectrum in Fig. 4.4 with an Ericson parameter of $\Lambda \cong 25$. About 1000 Fano-resonances, with an average width of $\bar{\Gamma} = 5$ meV, are randomly distributed in an energy region of 200 meV, and this spectrum was convoluted with a Gaussian function of 1.5 meV (FWHM). It should be mentioned that the intensities of all resonances are random, i.e. they are comparable.

Ericson [26] predicted that spectra with Ericson fluctuations display a autocorrelation function, $C(\varepsilon)$,

$$C(\varepsilon) = \frac{1}{\bar{\sigma}^2} \int_{E_1}^{E_2} \left[\sigma(E + \varepsilon) - \bar{\sigma}\right] \left[\sigma(E) - \bar{\sigma}\right] dE, \qquad (4.7)$$

with a Lorentzian form. Here, $\bar{\sigma}$ is the average cross section in the energy interval $E_1 \leq E \leq E_2$ and ε the displacement. From these autocorrelation function one can estimate the average width of resonances by a fit analysis. So far, it became a common method to analyze fluctuating spectra not only in the case of nuclear reactions [72] but also in

atomic scattering [16, 73]. Finally, we have to emphasize that an autocorrelation function with a Lorentzian form cannot be considered as an unambiguous evidence for Ericson fluctuations in a spectra. For a clear confirmation of Ericson fluctuations one has to ensure that the intensities of the resonances are randomly distributed. By neglecting this, one can easily to obtain wrong conclusions about the existence of Ericson fluctuations; this topic will be addressed in more details in combination with our TCS data in the Sect. 4.5.

4.3   The classical configurations

In the past 30 years, a modern semiclassical theory was developed to understand quantum chaos with the help of classical configurations. From the Bohr-Sommerfeld quantization condition, we know that there exits a strong classical-quantum correspondence in integrable systems. M. Gutzwiller [7, 8] realized that it is impossible to use a Bohr-Sommerfeld type of quantization to deal with chaotic systems. He introduced an entirely new semiclassical approach that abandoned the attempt to find individual chaotic states. A remarkable result of these considerations is Gutzwiller's trace formula [7, 8], which establishes a bridge between quantum states and classical periodic orbits, i.e. this formula can be utilized to calculate the density of quantum states from classical periodic orbits in a chaotic system and vice versa. These classical periodic orbits can be identified using a Fourier transformation of the quantum spectra. So far, one realizes that strong classical-quantum correspondences exist even in chaotic systems. However, this issue is beyond the topics in this dissertation. In the following, we shall introduce three classical configurations, which are necessary to understand the changes of approximate quantum numbers $N, K_{n'}$. These quantum numbers will be used to assign doubly excited resonances in helium as discussed before.

For doubly excited states in helium, the following three configurations in the classical space are of particular interests:

$$
\begin{array}{lll}
(A) & \text{eZe configuration:} & \theta_{12} \equiv \pi; \ \ p_{\theta_{12}} \equiv 0 \\
(B) & \text{Zee configuration:} & \theta_{12} \equiv 0; \ \ p_{\theta_{12}} \equiv 0 \\
(C) & \text{Wannier ridge:} & r_1 \equiv r_2; \ \ p_{r_1} \equiv p_{r_2}.
\end{array}
\tag{4.8}
$$

r and p are the coordinates and the momenta of electrons, respectively, while 1 and 2 label two different electrons, and θ_{12} is the angle between two electrons. (A) and (B) are collinear configurations, i.e. all particles move on one line; this is equivalent to a one-dimensional helium atom.

In the collinear configuration (A), all three particles move along one axis, with both electrons on opposite sides of the nucleus. It is called *eZe* configuration and shown in Fig. 4.5(b). In contrast to the *eZe* configuration, the *Zee* configuration, shown in Fig. 4.5(a), describes a motion with both electrons on the same side of the nucleus. The configuration (C) is a Wannier ridge, which shows the symmetric electron motion in a symmetry plane. The resonances corresponding to Wannier classical orbits are expected to appear only
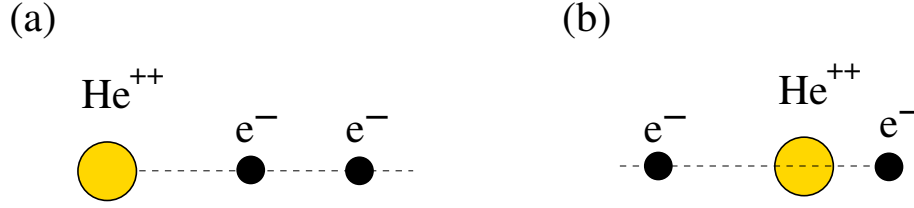
Figure 4.5: The two collinear configurations: (a) the stable *Zee* configuration and (b) the *eZe* configuration, which is chaotic in radial direction.

in the limit of double excitation very close to the double-ionization threshold [2, 74, 75]. The Wannier ridge, together with the *eZe* configuration, is predicted to contain the decay channels for double-ionization [76]. For detailed studies of the dynamics of these classical configurations, see Ref. [2] and references, therein.
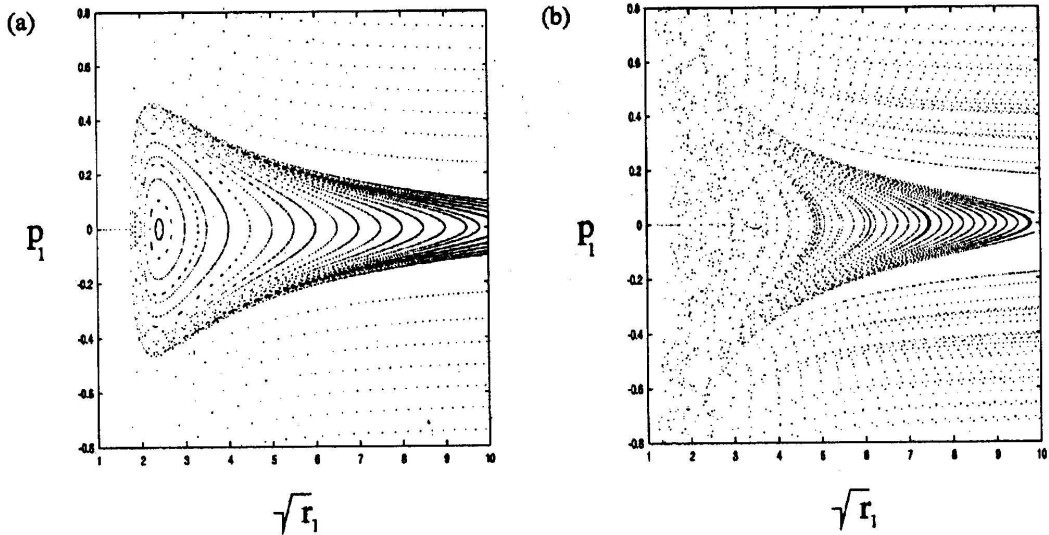

Figure 4.6: Poincaré map of helium for the two collinear configurations at $r_2 = 0$: (a) $\theta = 0$; (b) $\theta = \pi$ (taken from Ref. [2]).

Choosing $r_2 = 0$, one plots the phase space (Poincaré map) of the two collinear configurations in Fig. 4.6, i.e. the momentum of the outer electron is given as a function of its position. In the *Zee* configuration, surprisingly, the three-body Coulomb interaction leads to a stabilization of the dynamics in helium, which can be demonstrated well by a large stable island in the Poincaré map given in Fig. 4.6(a) [77]. The large stable island indicates that the outer electron in the *Zee* configuration is frozen at a finite distance from the nucleus, i.e. the outer electron cannot penetrate the inner electron and, therefore, cannot hit the nucleus. Due to the electron-electron and electron-nucleus interactions, the outer electron performs an oscillation at a frozen distance. In contrast, the inner electron can move between the nucleus and the outer electron. Therefore, the *Zee* is a quite stable configuration. In contrast to the stable *Zee* configuration, no stable islands can be found in the *eZe* configuration in the Poincaré map given in Fig. 4.6(b), particularly as $r_1 \to 0$, where the Poincaré map is completely structureless. In

this configuration, triple collision ($r_1 = r_2 = 0$) can occur. This, in turn, results in large momentum transfer among the three bodies (two electrons and the nucleus), and has been considered as the origin of chaos in the eZe configuration.

In summary, for perturbations in the direction of the electron-nucleus axis, the 1-dimensional helium is unstable in the eZe configuration but stable in the Zee configuration. Both configurations are stable with respect to perturbations perpendicular to the collinear phase space, i.e. stable in the angular direction. In this dissertation, the two classical configurations eZe and Zee will be employed to understand the existence and loss of the approximated quantum numbers $N, K_{n'}$, where N and n' (K) describe the radial (angular) directions.

4.4 Complex-rotation method

As we mentioned before, the statistical studies were performed using the theoretical results D. Delande obtained with the complex-rotation method. This procedure is due to the extremely low intensity of most of the Rydberg series which give rise to the fact that only a very small fraction of doubly excited states can be observed experimentally. Therefore, the complex-rotation method will be described briefly.

The method of complex-rotation [78, 79] is quite different with other methods in determining the resonant state; normally, these resonances are obtained by diagonalization of a Hamiltonian matrix. The difference of the complex-rotation method is due to the complex scalings of the radial coordinates and momenta, $r \rightarrow re^{i\theta}$ and $p \rightarrow pe^{-i\theta}$. In this way, the expectation value of the Hamiltonian becomes

$$\langle n_\theta | H | n_\theta \rangle = E_n - i\Gamma_n/2, \tag{4.9}$$

where $|n_\theta\rangle$ is the complex scaling wave function for the double-excitation states, and E_n and Γ_n represent the positions and the linewidths of resonances, respectively. The dipole transition matrix has the complex form

$$\langle i | D | n_\theta \rangle = B_n + iC_n, \tag{4.10}$$

with $|i\rangle$ being the ground state. Using the complex parameters B_n and C_n together with E_n and Γ_n, the Fano-shape parameterization of the cross section yields

$$\sigma_T = \sigma_T^0 + \sum_n \frac{(q_n + \epsilon_n)^2}{1 + \epsilon_n^2} \mu_n^2 - \mu_n^2, \tag{4.11}$$

where

$$\epsilon_n = 2\frac{E - E_n}{\Gamma_n},$$

$$q_n = -\frac{B_n}{C_n},$$

$$\text{and} \quad \mu_n^2 = \frac{2C_n^2}{\pi\Gamma_n}. \tag{4.12}$$

The cross section and Fano parameters can be directly derived from the two matrix elements given in Eqs. 4.9 and 4.10. This is a substantial advantage of the complex-rotation method compared to other methods, since the resonant parameters E_n, Γ_n, and q_n as well as the expectation value $\langle cos\theta_{12}\rangle$, can be obtained directly from calculations; they do not have to be derived by a fit analysis of the calculated cross section, which is impossible in the present case of strongly overlapping resonances. The value $\langle cos\theta_{12}\rangle$ is related to the approximate quantum number K by Eq. (3.16). Therefore, the complex-rotation method is very well suited to provide data for statistical studies of the resonant parameters E_n, Γ_n, and q_n.

In the late 1990's, complex scaling photoabsorption calculations for helium performed by Gremaud and Delande [32] covered the energy regime up to the SIT I_9 and have been used by our group to perform statistical studies on the NNSs of energy levels in that region [18]. Very recently, Delande [27] further extended these calculations up to the SIT I_{17}, i.e. up to 150 meV below the double-ionization threshold of helium. These calculated data will be employed for the studies of quantum chaos in the next section of the dissertation.

4.5 Quantum signatures of chaos in highly excited states of helium

4.5.1 Experimental total cross sections up to I_{15}

The high-resolution photoionization spectra presented in Fig. 4.7 were measured up to the SIT I_{15} using a gas cell described in chapter 2. The experiments were performed at the high-resolution undulator beamline UE56-2/PGM2 of the Berliner Elektronen-speicherring für Synchrotronstrahlung (BESSY II) using a photon energy resolution of $\Omega \cong 1.7$ meV (FWHM). A pressure of $\cong 1$ mbar was used in the gas cell, and an operating voltage of 100 V was applied to the plates within the gas cell. The spectra were taken with a step width of 250 μeV, and six scans were recorded for each energy region in order to ensure reproducibility and to improve the signal-to-noise ratio. The backgrounds of the spectra were simulated and subtracted from the spectra. The photon energies of the spectra were calibrated by the result of the calculations of Delande [27].

In Fig. 4.7, the present experimental data, and the results of theoretical calculation employing the complex-rotation method [27], as well as the results of previous measurements by Püttner *et al.* [18] for the TCSs are plotted as solid lines in three different colors. The vertical bars mark the positions of the SITs up to I_{14}. The theoretical data were convoluted by a Lorentzian function with a FWHM of 1 meV. A comparison of the recent experimental and theoretical results shows an impressively good agreement for the entire spectrum. The present spectra show an improved signal-to-noise ratio and higher resolution than the previous measurements [18]. The present experimental and theoretical data above 78.28 eV are the first ones in this energy region, i.e. data below 6 new ionization thresholds were obtained. The complex features the spectra indicate
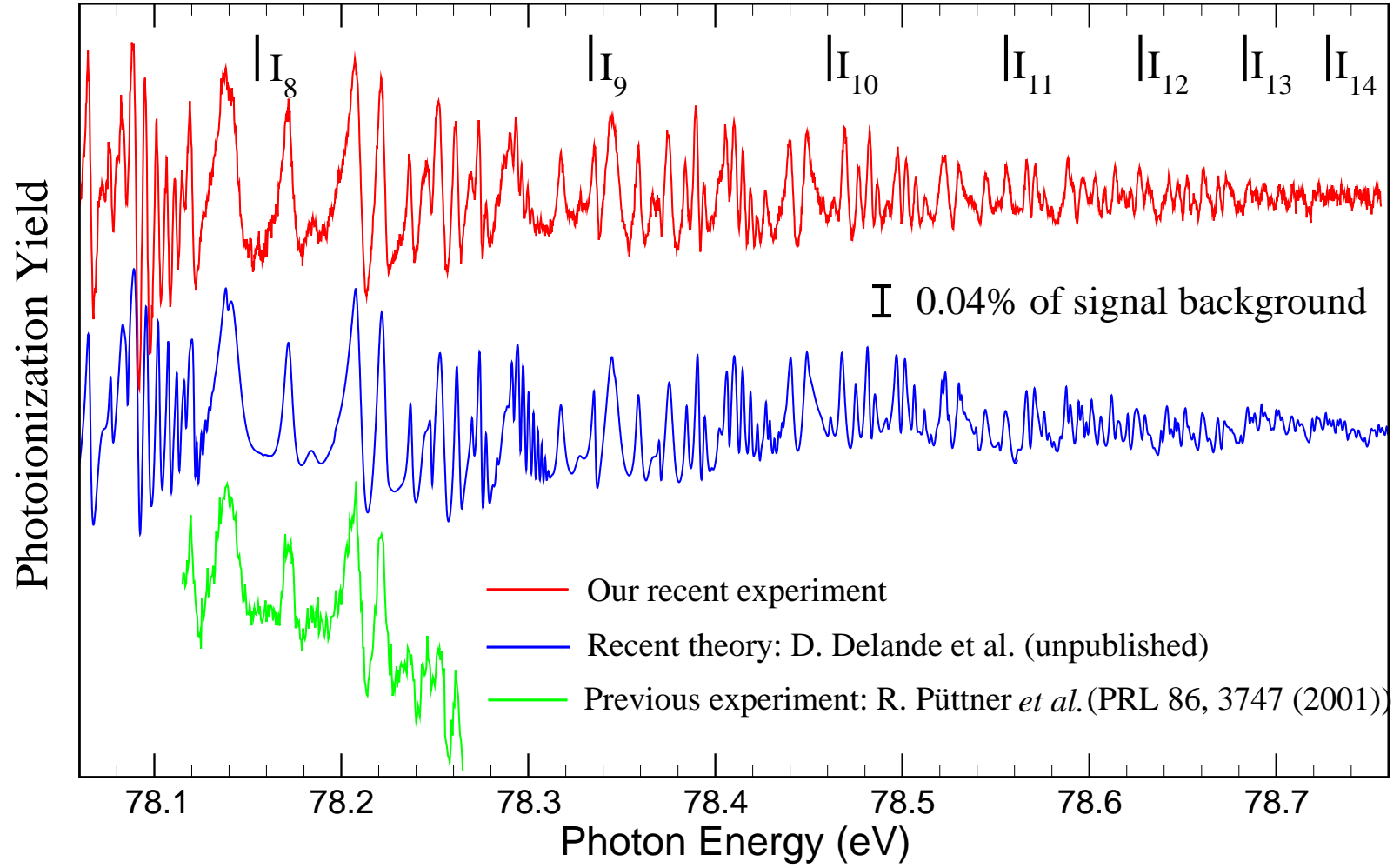
Figure 4.7: Total cross section of doubly excited helium below the SIT I_{15}. The present experimental data, complex-rotation calculations [27], and previous measurements [18] are plotted by solid lines in red, blue, and green colors, respectively. The vertical bars indicate the positions of the SITs up to the I_{14}.
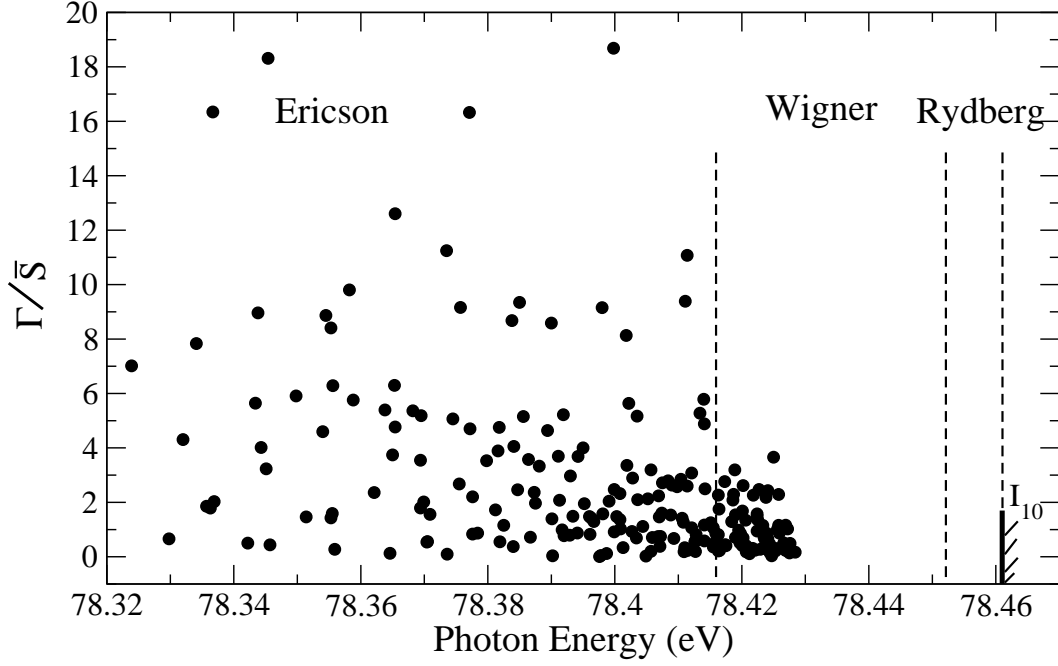
Figure 4.8: Calculated linewidths of doubly excited states in helium below the SIT I_{10}. The resonance linewidths are normalized to the mean value of spacings between the resonance energy positions. Ericson ($\overline{\Gamma} \gg \overline{S}$), Wigner ($\overline{\Gamma} \approx \overline{S}$), and Rydberg ($\overline{\Gamma} \ll \overline{S}$) regimes are indicated.

in the presence of a large number of perturbers in this energy region. These perturbers render the spectra significantly irregular (see Fig. 3.3) and it is therefore an interesting question whether or not the spectra can be assigned with isolated resonances. From the experimental point of view, it is really hard to take spectra in this energy region because the amplitudes of the resonances amount to only 0.2% to 0.04% of the signal background. The variations in the pressure and insufficient normalization to the photon flux could render the observation of these resonances impossible. From the theoretical point of view, many challenges are also faced due to the calculation model, accuracy, and convergence. The present state-of-the-art measurements and calculations of the TCS make it possible to study for the first time chaotic behavior in doubly excited helium very close to double-ionization threshold. The theoretical data obtained by D. Delande [27] are strongly confirmed by the present measurements and can be used as a reliable basis for further data analysis. As mentioned before, we have to use theoretical data for these detailed statistical studies because only a relatively small number of resonances can be observed in the experiments; this will be further illustrated by our fit results described in the following section.

Close to the double-ionization threshold, the mean linewidth of the resonances is much larger than the mean spacing of the resonances, i.e. $\overline{\Gamma} \gg \overline{S}$ (Ericson regime), where the resonances are strongly overlapping. In this case, the spectra are assumed to fluctuate and cannot be identified. Generally, the Ericson regime together with the comparable intensities of the spectra are assumed to be the conditions for observing Ericson fluctuations in the spectra as mentioned in Sect. 4.2. In this part, the main aim
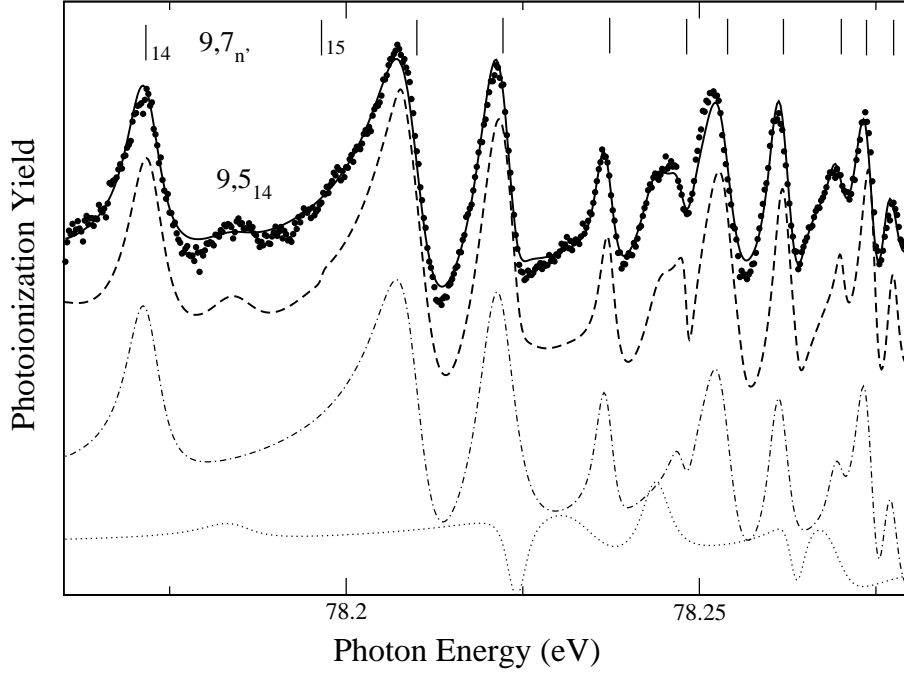
Figure 4.9: Total cross section below the SIT I_9: The present experimental data are given by solid points, the fit result by the solid curve through the data points. The result of the complex-rotation calculations is given by the dashed curve. The fit components for the principal and secondary Rydberg series are represented by the dash-dotted and dotted lines. The vertical-bar diagrams in the upper part of the figure give the assignments of the resonances belonging to the Rydberg series $9, 7_{n'}$.

of the analysis of the experimental data is to figure out whether Ericson fluctuations are present in the studied energy region. In Fig. 4.8, the normalized linewidths of doubly excited states in helium below the SIT I_{10} are plotted as a function of photon energy. These linewidths are normalized to the mean value of the spacings between the resonance energy positions. These data were calculated with the complex-rotation method by D. Delande [27]. There are three classes of resonances below each SIT, which can be identified by a comparison of the linewidths and energy level spacings. They are, in the order of increasing energy, Ericson ($\overline{\Gamma} \gg \overline{S}$), Wigner ($\overline{\Gamma} \approx \overline{S}$), and Rydberg ($\overline{\Gamma} \ll \overline{S}$) regimes, respectively, which have been identified below I_{10} and are indicated in Fig. 4.8. Later, the analysis of experimental spectra will focus on the region, where the corresponding resonances are in the Ericson regime, i.e. $\overline{\Gamma} \gg \overline{S}$.

A detailed comparison between the experimental and theoretical TCSs in the region up to the SIT I_{14} are given in Figs. 4.9 to 4.14. In these figures, the experimental TCSs are plotted as solid points and the dashed lines represent the theoretical results. The fit results are displayed by solid lines through the data points. As an example, the contributions of individual resonances for the principal and secondary Rydberg series are plotted by dash-dotted and dotted lines, respectively, in the lower part of Fig. 4.9. The vertical bars in the upper part of each figure mark the energy positions of the resonances. In the fit process, we fixed the resonance positions, linewidths, and Fano parameters q to
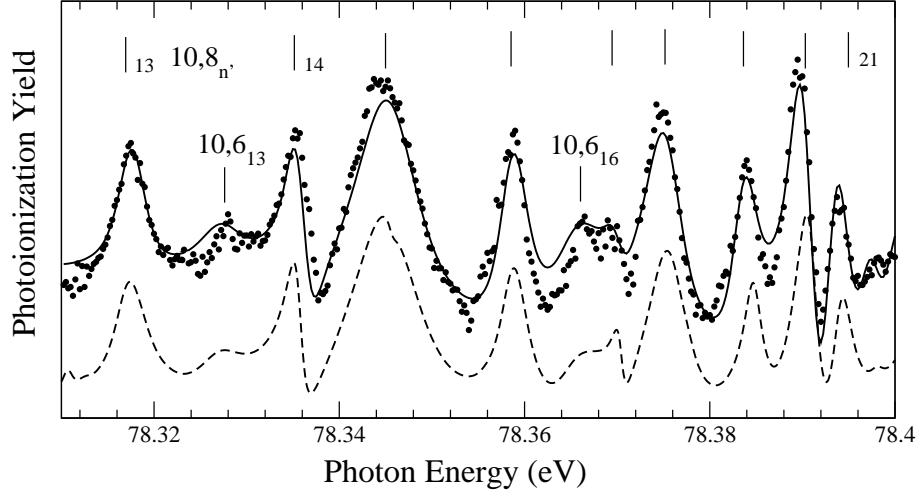
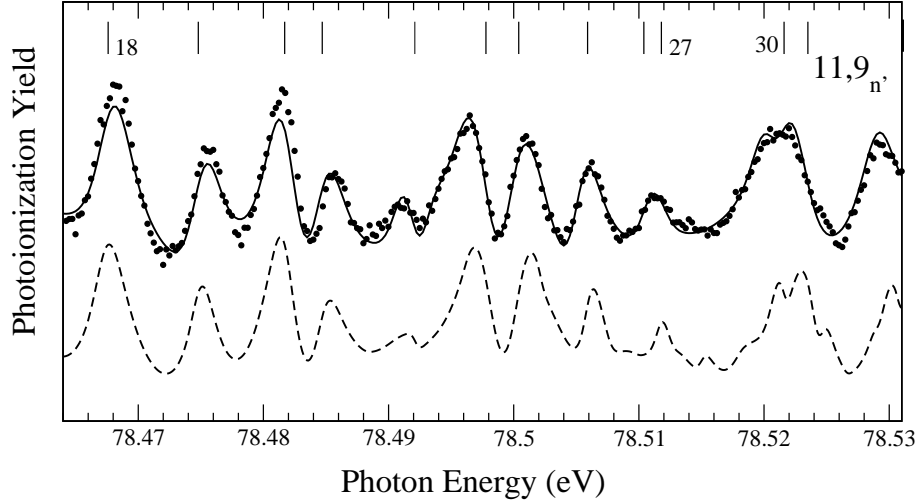Figure 4.10: Total cross section below the SIT I_{10}. For details, see caption of Fig. 4.9.

Figure 4.11: Total cross section below the SIT I_{11}. For details, see caption of Fig. 4.9.

the values of the calculations by D. Delande [27]. The intensities are treated as the only free parameters and the obtained relative intensities for most of the resonances agree with the calculated ones within a factor of 2. Due to possible tiny mechanical problems of the used monochromator [80], which could lead to small non-linearities, the photon energies of the individual resonances were allowed to have shift linearly up to 1 meV. The aim of the fits is to determine the number of resonances that are needed to reasonably describe the spectra. This is closely related to the question whether Ericson fluctuations are present in this region of the spectrum or not. Therefore, the spectra are described by fit routines using the smallest number of resonances, which lead to a sufficiently good description; such a fit procedure can be called "describing fit".

For the spectra below the SITs I_9 to I_{14}, 15 to 25 resonances were used in the describing fits. Most of these resonances can be assigned to members of the principal series ($K = N - 2$), while a much smaller fraction belongs to the secondary series ($K =$
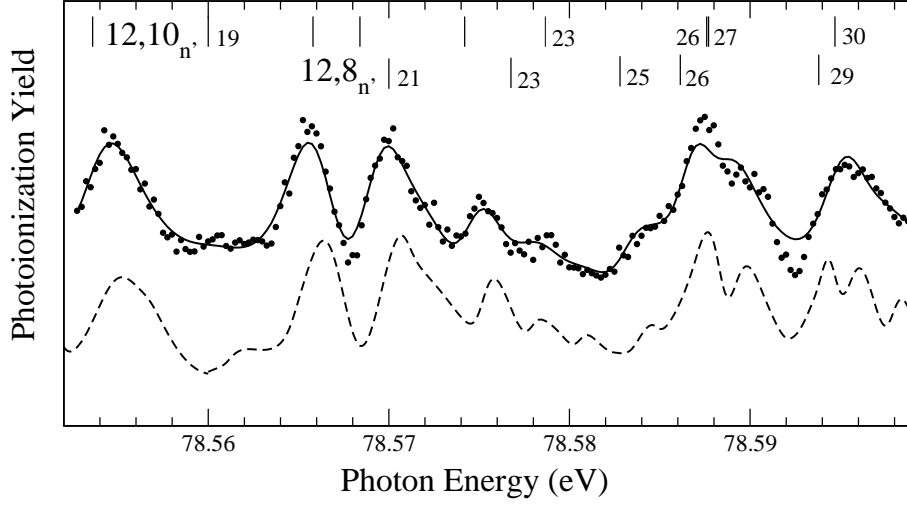
Figure 4.12: Total cross section below the SIT I_{12}. For details, see caption of Fig. 4.9.
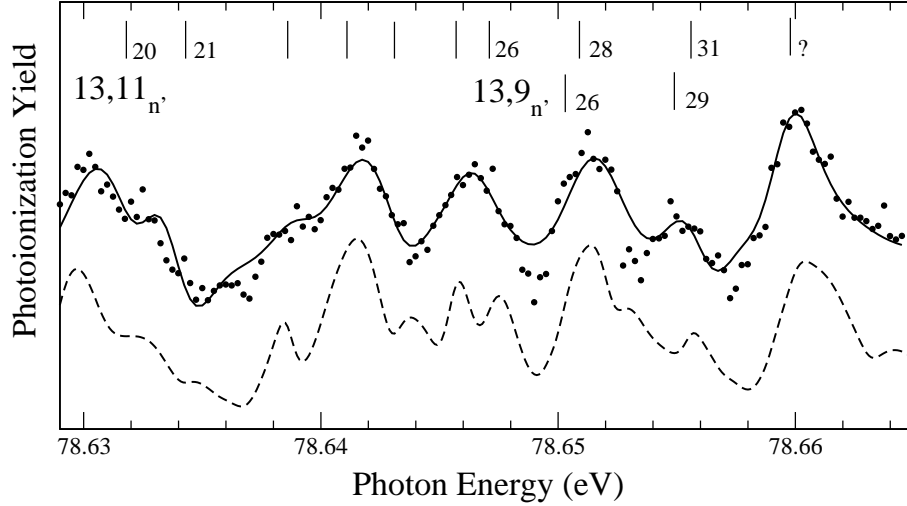

Figure 4.13: Total cross section below the SIT I_{13}. For details, see caption of Fig. 4.9.

$N-4$); this can be seen from the fit components shown in Fig. 4.9, as an example. With these finite numbers of resonances, the experimental spectra can already be described quite well. Note that there are $17-27$ Rydberg series with more than 300 resonances in the corresponding energy regions below each of the SITs I_9 to I_{14}. In addition, we point out again that Fig. 4.8 gives clear evidence that the spectra studied in this dissertation are in the Ericson regime, i.e. $\overline{\Gamma} \gg \overline{S}$. However, the present describing fits indicate clearly that the spectra are still dominated by essentially a single Rydberg series, namely the principal series ($N = K - 2$); this means that Ericson fluctuations caused by a large number of overlapping resonances are essentially absent in the spectra. This indicates that some approximate quantum numbers $N, K_{n'}$ should be still valid, a fact that will be proven later on by analyzing the calculated K values and by a statistical analysis of energy spacings between the resonances. So far, we can conclude that the Ericson
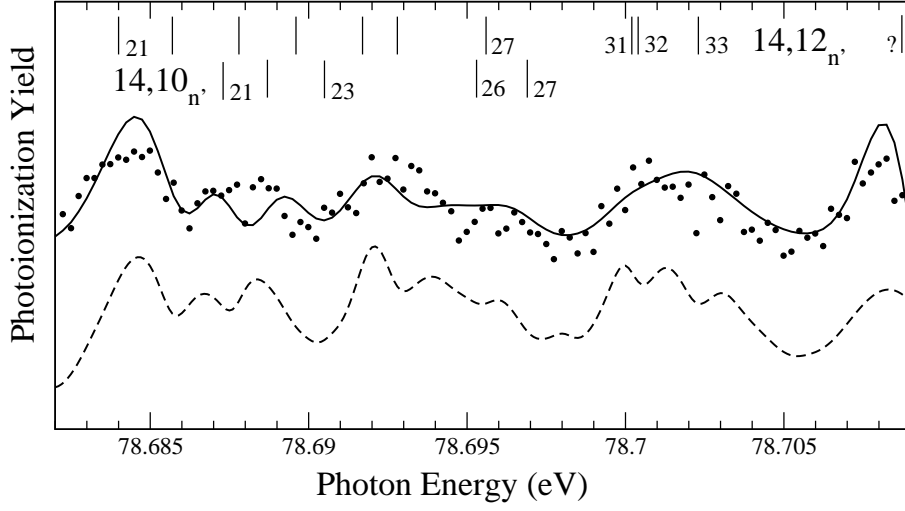
Figure 4.14: Total cross section below the SIT I_{14}. For details, see caption of Fig. 4.9.

regime is not a unique condition for observing Ericson fluctuations in the spectra. The amplitudes of transitions have to be distributed randomly.

We further point out that the agreement between the measurements, the fits, and the calculations becomes worse with increasing photon energies according to the increasing noise. On the basis of the describing fits and theoretical data, we assigned for the first time the experimental spectra up to the SIT I_{14} . The symbol "?" in Figs. 4.13 and 4.14 implies that a particular resonance could not be identified since its K-value could not be obtained from the calculations due to convergence problem. The theoretical convergence problem close to each SIT does not affect the reliability of the TCS [27], however. Due to missing resonance parameters close to each SIT, it was not possible to analyze the entire spectrum presented in Figs. 4.7 by the describing fits, which are presented in Figs. 4.9 to 4.14.

Although it has been proven that Ericson fluctuations are absent in the present spectrum, in the following we want to discuss its autocorrelation function since such a autoionization function was employed by G. Stania and H. Walther [16] as an evidence for Ericson fluctuations in the photoionization spectra of ^{85}Rb atom. To this end we compare the TCS of helium without Ericson fluctuations in Fig. 4.9 with a simulated spectrum in Fig. 4.4 that clearly displays Ericson fluctuations. We first want to point out that these two spectra exhibit similar features so that it is not possible to identify Ericson fluctuations by the variations in the cross section. For these both spectra the autocorrelation functions defined by Eq. (4.7) are calculated and presented in Fig. 4.15(a) and (b). The dashed lines in this figure are the results of a fit to a Lorentzian function, which is prediction for Ericson fluctuations. For small displacements, i.e. ε close to 0, the autocorrelation functions agree quite well with the Lorentzian function. For larger displacements, oscillations around zero are observed. The average widths of resonances of $\cong 2$ and 5 meV for the spectra in Figs. 4.9 and 4.4, respectively, are in good agreement with the ones of $\cong 3$ and $\cong 4$ which were derived from the fits. The observed features of the autocorrelation function are quite similar to that observed by G. Stania
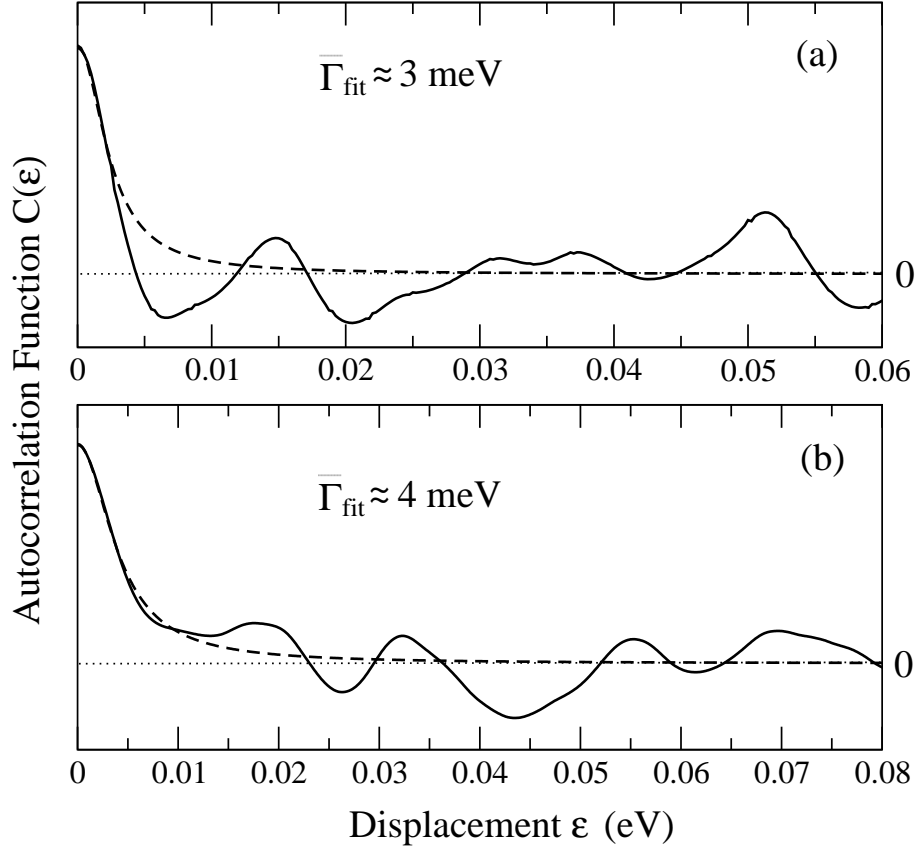
Figure 4.15: (a) Autocorrelation functions for the spectra given in Fig. 4.9 and (b) in Fig. 4.4. The dashed lines represent the fit results to a Lorentzian function, and the dotted horizontal lines indicate the value of zero.

and H. Walther. As stated before, the TCS given in Fig. 4.9 does not exhibit Ericson fluctuations. This is due to the fact that the spectrum is dominated by the principal Rydberg series although the Ericson regime ($\Lambda = \bar{\Gamma}/\bar{S} \cong 3$) is fulfilled. In addition, for small ε the autocorrelation function displays a Lorentzian shape (see Fig. 4.15(a)). Similar autocorrelation functions were also found for the TCSs in the other regions up to I_{13} where the Ericson parameter, Λ, has larger values. These considerations show that Ericson fluctuations in a spectrum can neither be identified by the shape of the spectral variations nor by the autocorrelation function. It is, therefore, essential to ensure that the intensities are also randomly described with a large number of overlapping resonances. Nevertheless, the average width of the resonances in a fluctuating spectrum can be estimated by fitting the autocorrelation function to a Lorentzian function; this can be seen from our simulated chaotic spectrum in Fig. 4.4 as well as its autocorrelation function in Fig. 4.15(b).

In the work of G. Stania and H. Walther [16] as well as J. Madronero and A. Buchleitner [17], an autocorrelation function with a Lorentzian shape for small displacements was used to prove the observation of Ericson fluctuations. However, the the question of comparable amplitudes for the transitions was not carefully addressed. The present case of helium shows that this omission may lead to wrong conclusions if there is – contrary

to an assumption – an unexpected hierarchy in the intensities of the different resonances.

4.5.2 Calculated K values up to I_{17}

In the last section, we concluded from the describing fits that Ericson fluctuations do not occur although the conditions for the Ericson regime is fulfilled, as shown in Fig. 4.8; i.e. the spectra are still dominated by the principal series $N, K_{n'}$, with $K = N - 2$, at least up to the SIT I_{14}. The spectral features in this energy region were assigned using the approximate quantum numbers $N, K_{n'}$. However, this does not mean that approximate quantum numbers are still valid for all resonances. As mentioned before, the complex-rotation method has the advantage that the K values for each resonance can be calculated directly. With this theory, Delande [27] has performed calculations for K values up to the SIT I_{17}, as well as for the TCS below the SIT I_{14}. The accuracy of these calculations is confirmed by our recent experimental results as discussed in the previous section. Here, we shall discuss the approximate quantum numbers $N, K_{n'}$ on
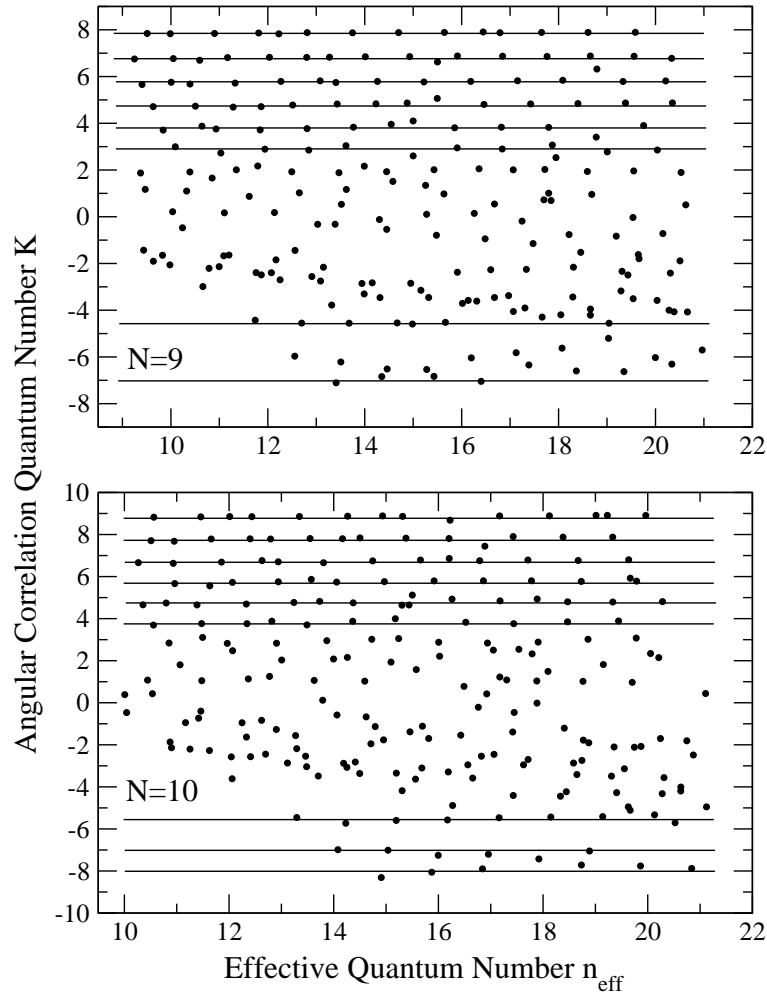

Figure 4.16: Angular correlation quantum numbers K calculated by D. Delande [27] below the SITs I_9 and I_{10} as a function of effective quantum number. Each point represents one resonance and the horizontal lines imply Rydberg series specified by individual K values.
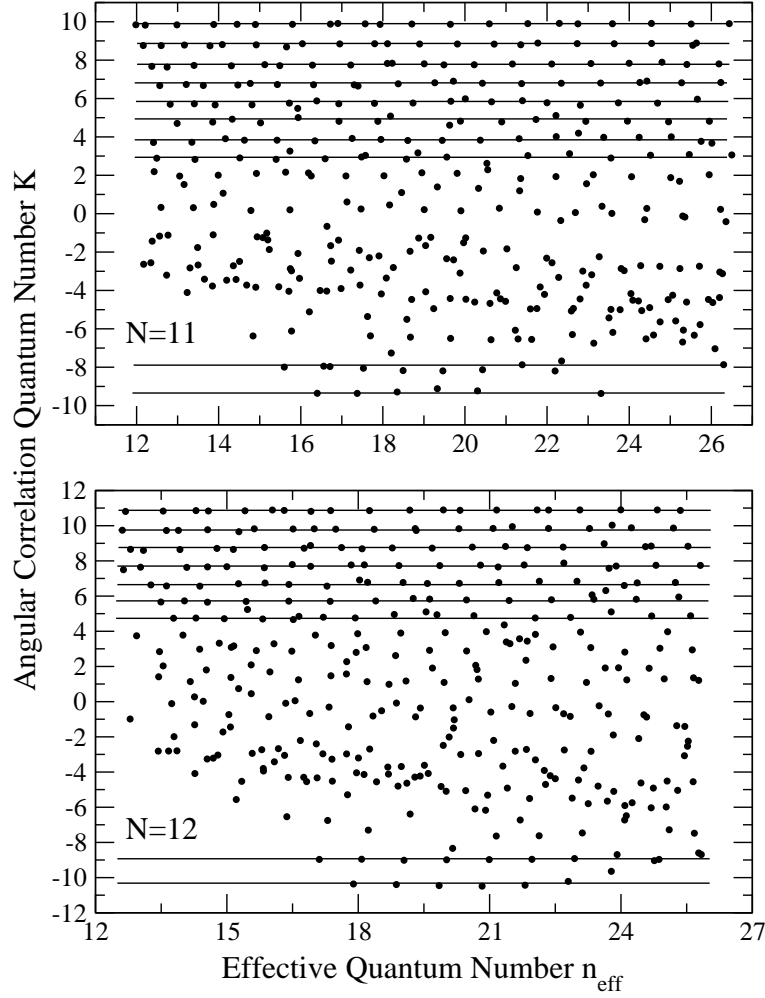
Figure 4.17: Calculated angular correlation quantum numbers K below the SITs I_{11} and I_{12} as a function of the effective quantum number. For details, see Fig. 4.16.

the basis of reliable K values. This will help to understand the statistical properties of the NNSs between the resonances, which will be presented in the next section.

The calculated angular correlation quantum numbers K for the doubly excited resonances from the SITs I_8 to I_{17} as a function of the effective quantum numbers n_{eff} are plotted in Figs. 4.16 to 4.20. Each solid point in these figures represents a resonance specified by the K-value and the energy given in units of the effective quantum number. The horizontal lines indicate Rydberg series, which can be identified by individual K values. The spectra were rescaled to the effective quantum numbers by Eq. (4.2) in order to study the radial quantum numbers N and n'. According to quantum defect theory [25], all resonances in a regular Rydberg series, which are specified by various n', should have the same quantum defect. This results in the energy level spacings to be equal to one on the rescaled energy axis, and implies the radial quantum numbers N and n' to be good quantum numbers. Otherwise, for irregular level spacings, N and n' are assumed to be strongly mixed, i.e. N and n' loose their meanings as the principal quantum numbers of the inner and outer electron in an independent particle picture.
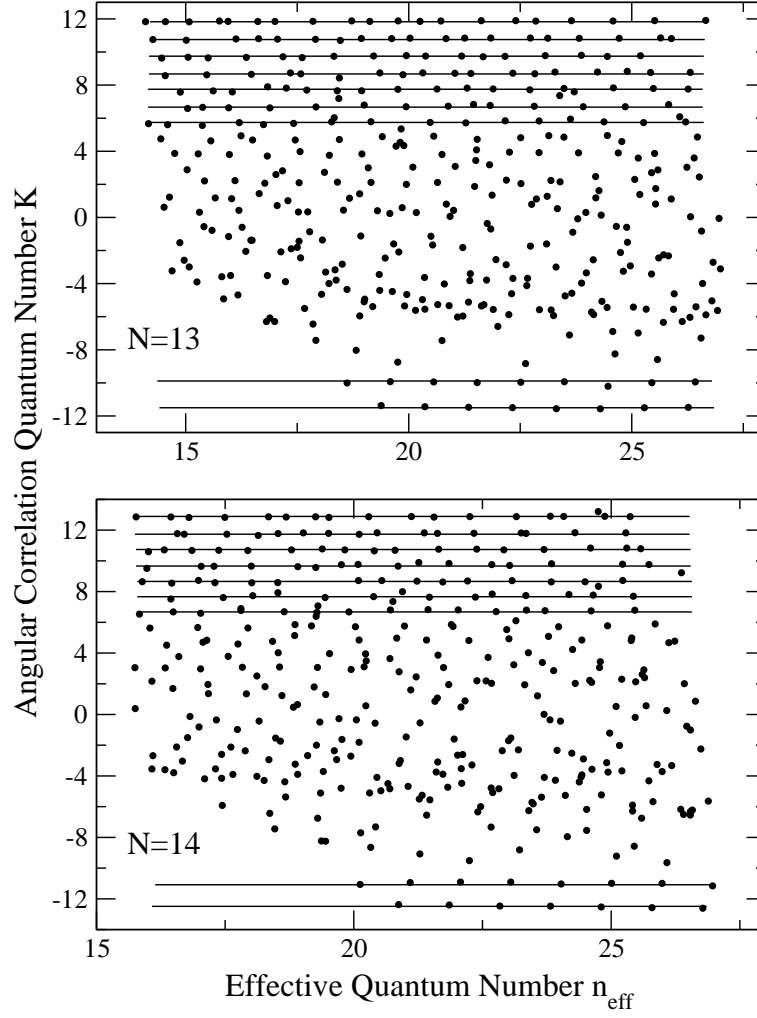
Figure 4.18: Calculated angular correlation quantum numbers K below the SITs I_{13} and I_{14} as a function of the effective quantum number. For details, see caption of Fig. 4.16.

From these figures it can be clearly seen that−for the resonances with K values close to K_{max}−the angular correlation quantum number K has well-defined value. This is indicated by horizontal lines in Figs. 4.16 to 4.20 and allows to define independent Rydberg series. Therefore, in these cases K can be considered to be a good quantum number. The second top horizontal lines represent the principal series with $K = N − 2$ below the various SITs, I_N. From the expression (3.16), the angle between two electrons $\theta_{12} \to 180°$ as $K \to K_{max}$, and this corresponds to the classical eZe configuration. As discussed in Sect. 4.3, this configuration is stable towards a perturbation in the angular direction, which results in K being a good quantum number. Therefore, theoretical results for K values agree well with this prediction for the eZe configuration. The energy level spacings of the resonances, which belong to the Rydberg series with constant K, are irregular; they are not equal to unity, which indicates that the radial quantum numbers N and n' start to dissolve for these Rydberg series. This can also be understood by the classical eZe configuration, since this configuration is unstable against perturbations along the axis defined by the two electrons and the nucleus. Interestingly, the number
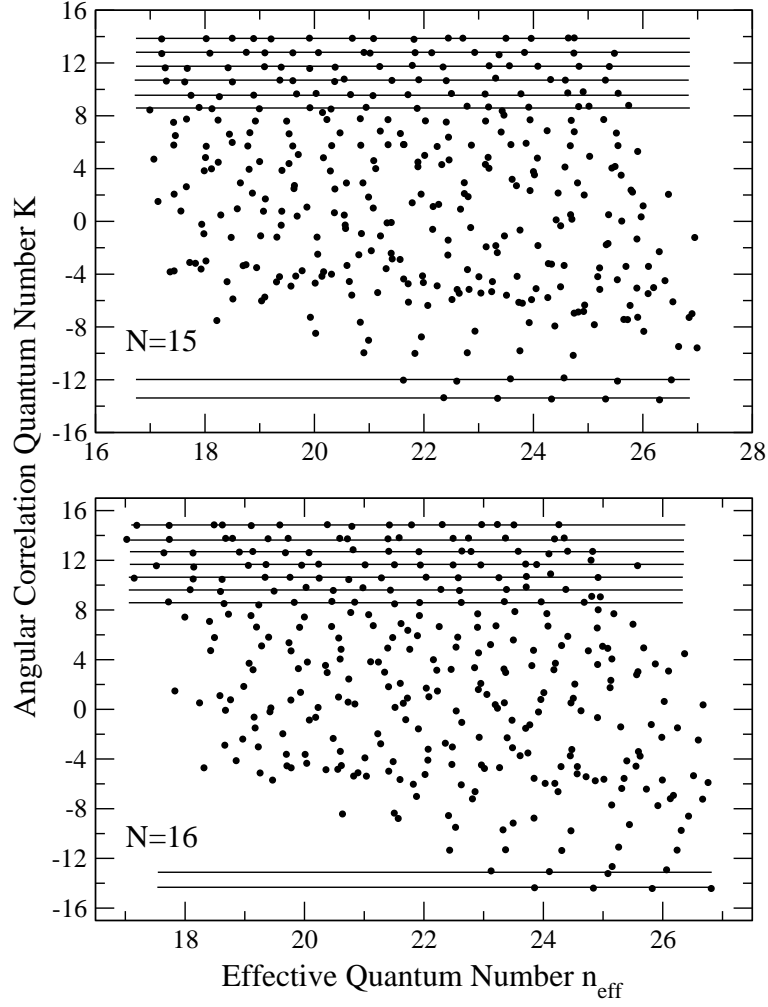
Figure 4.19: Calculated angular correlation quantum numbers K below the SITs I_{15} and I_{16} as a function of the effective quantum number. For details, see caption of Fig. 4.16.

of Rydberg series with good K values in the region of $K \rightarrow K_{max}$ does not decrease dramatically up to the SIT I_{17} as expected before. The basis for this expectation was the assumption K could break down rather quickly above the SIT I_9.

K is also found to be a good quantum number for Rydberg series in the region of $K \rightarrow K_{min}$, in particular for the higher photon energy region above the SIT I_{10} (see Figs. 4.17 to 4.20). This is indicated by horizontal lines in the lower parts of the figures. In addition to that, the energy level spacings of these Rydberg series are always close to one, which proves that the radial quantum numbers N and n' are good quantum numbers. $\theta_{12} \rightarrow 0°$ and $K \rightarrow K_{min}$ correspond to the classical *Zee* configuration. The *Zee* configuration is also identified by the *frozen planet* orbits [2] and is stable with respect to perturbations in both directions, namely the angular direction and the radial direction. Therefore, the classical *Zee* configuration allows us to understand why K and N are good quantum numbers for Rydberg series in the region of $K \rightarrow K_{min}$. Note that the calculations below the SIT I_{17}, shown in Fig. 4.20, were not yet completely carried out, i.e. only data for the effective quantum number $n_{eff} < 24$ are available
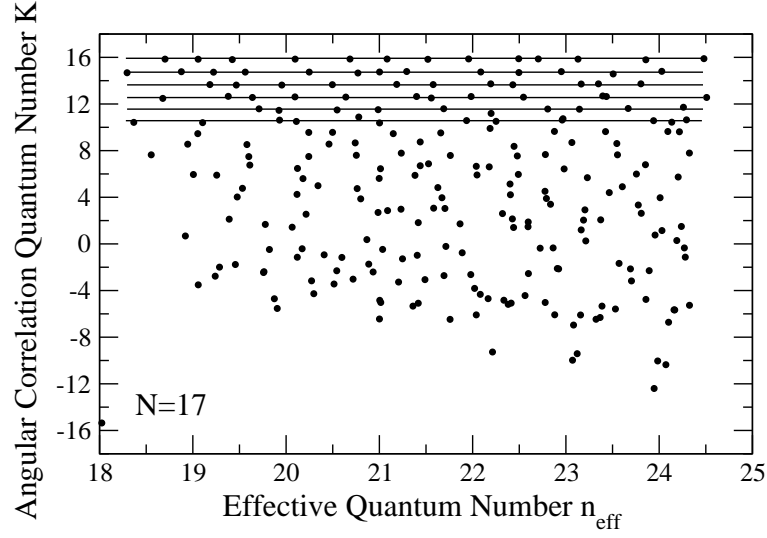
Figure 4.20: Calculated angular correlation quantum numbers K below the SIT I_{17} as a function of the effective quantum number. For details, see caption of Fig. 4.16.

at the moment. From the figures showing data for lower SITs, one can see that the corresponding Rydberg series with K_{min} values start at relatively high effective quantum numbers. This is the reason why the resonances for $K \rightarrow K_{min}$ are not yet available below the SIT I_{17}, but we expect them to have good K quantum numbers.

It is obvious from Figs. 4.17 to 4.20 that there is a strong mixing of K in the regions arround $K = 0$, i.e. $\theta_{12} \cong 90°$. More studies are needed to figure out the behavior of quantum number N. The present results on changes of the approximate quantum numbers $N, K_{n'}$ are in agreement with the discussion for $^1S^e$ doubly excited state of helium below the SIT I_{10} given by Bürgers *et al.* [81], but they explore the energy region much closer to the double-ionization threshold.

In Fig. 4.21, all calculated $\langle cos\theta_{12}\rangle$ below the SIT I_{17}, related to K-values by the expression (3.16), are plotted as a function of photon energy. The principal Rydberg series is marked by a solid curve through the resonance points. From this figure, one can clearly conclude that K does not break down as a good quantum number in the energy regions below the SITs I_9 to I_{17}, as expected before; this is particularly true for the regions $K \rightarrow K_{max}$. In addition, we note that the K values for the Rydberg series in the regions $K \rightarrow K_{max}$ increase slowly but constantly. This can be caused by the influences of perturbers with large K values that belong to Rydberg series below the next higher threshold. An increase is also observed at each threshold, which can be understood from the formula given in Eq. (3.16). The same data as in Fig. 4.21 are plotted in Fig. 4.22 in a polar coordinate representation. From this figure, we can see that K is a good quantum number for the regions $\theta_{12} > 100°$ and $\theta_{12} < 50°$, but mixes strongly in the region from $60° < \theta_{12} < 100°$. We note that θ_{12} for the resonances of the principal Rydberg series vary from the angles $135°$ to $150°$ in the present energy region. This energy-dependent angular correlation distribution of the principal Rydberg series is related to that of doubly ionized states, which will be presented later. The
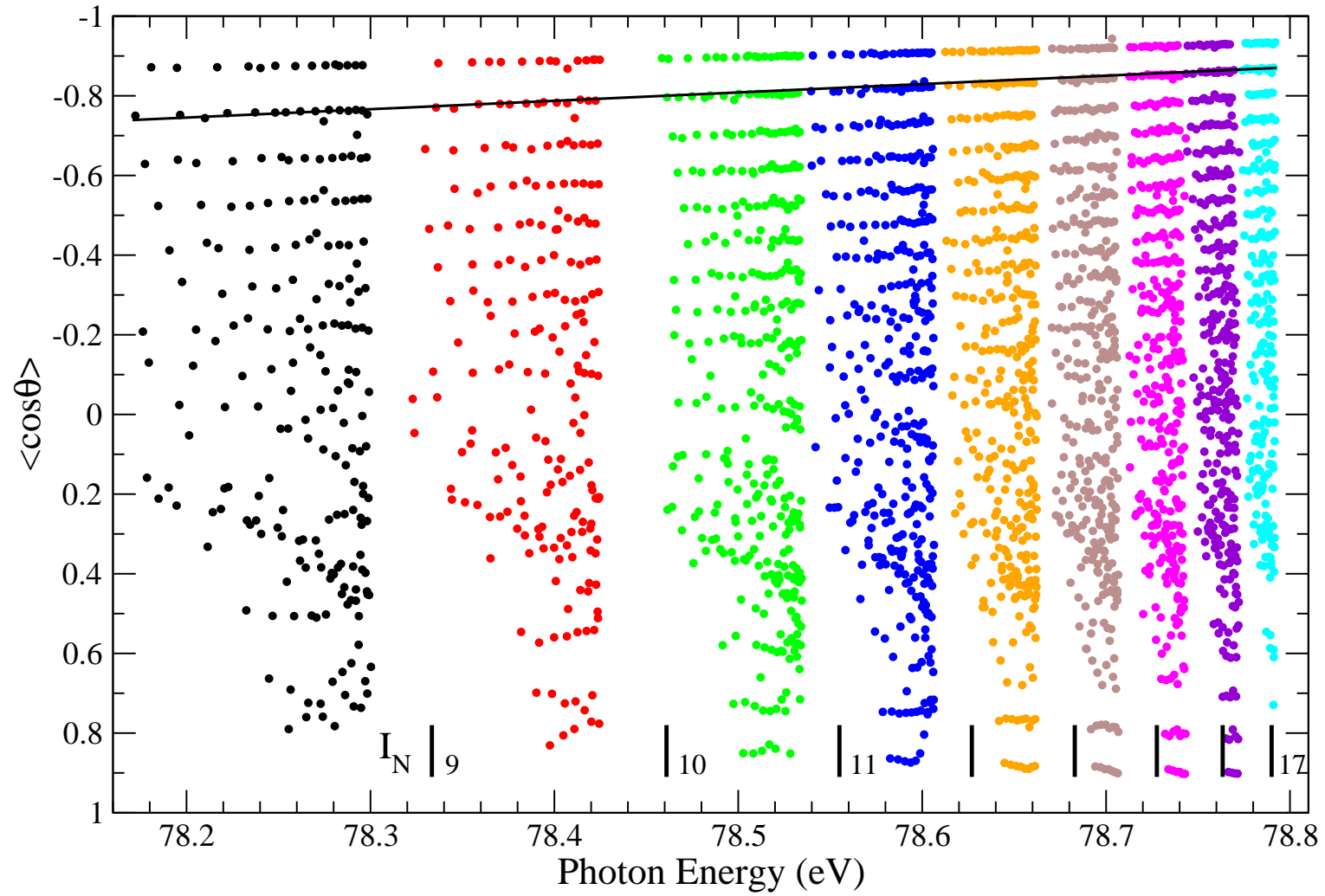
Figure 4.21: Calculated $\langle cos\theta_{12} \rangle$ values as a function of photon energy below the SIT I_{17}. Each point represents one resonance, and the positions of single photoionization thresholds I_N are marked by thick vertical bars in the lower part of the figure. The principal Rydberg series is indicated by a solid black line.
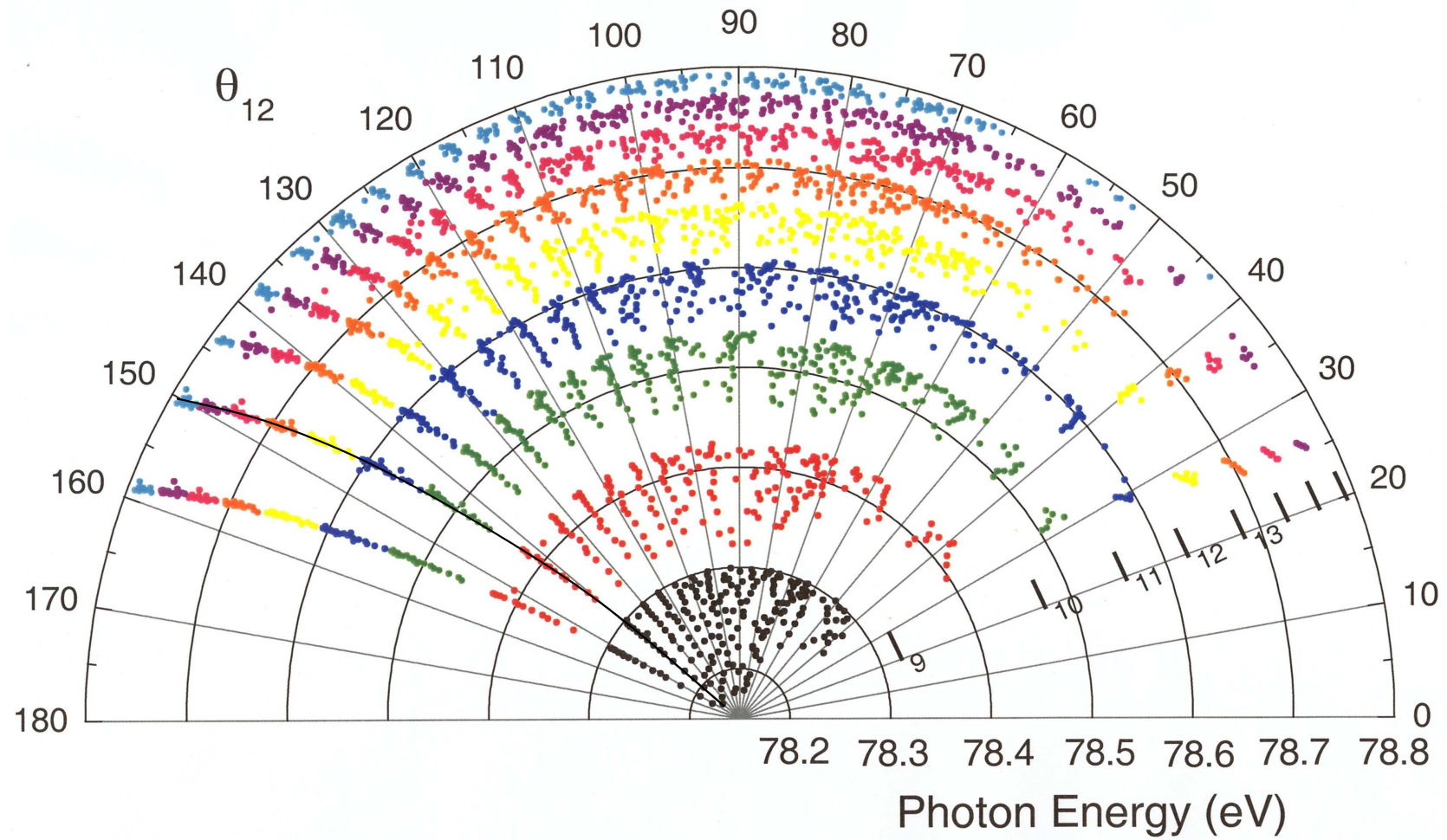
Figure 4.22: Calculated θ_{12} as a function of photon energy below the SIT I_{17} in a polar coordinate scheme. The principal Rydberg series is indicated by a solid black curve. This figure displays the same data as Fig. 4.21.

present discussion on the approximate quantum numbers N, K will be confirmed by the statistical analysis of the NNSs between resonances presented in the next section.

Under the assumption that all resonances are of comparable intensities, the cross section cannot be described by individual resonances. Instead, the cross section consists of fluctuations with a width equal to the typical linewidth, and it is composed of a large number of individual resonances. For helium, the prerequisite for Ericson fluctuations to be observed, which is the condition that the mean linewidth is much larger than the mean level spacing, is already fulfilled below the SIT I_9 [32]; this can be seen from an inspection of the data below the SIT I_{10} presented in Fig. 4.8. Therefore, the existence of Ericson fluctuations depends additionally on the condition that all resonances contribute equally to the spectra. From the previous discussion we know, however, that the spectra up to the SIT I_{14} are still dominated by the principal series ($K = N - 2$), and its K value is still a good quantum number. This is the reason why Ericson fluctuations cannot be found in this moment although the region concerned is in the Ericson regime. As mentioned before, we conclude in this dissertation it is very dangerous to discuss the Ericson fluctuations by an autocorrelation function fitted by a Lorentizian form before one is able to really comfirm the prerequisites of the Ericson fluctuations, in particular for comparable intensities of resonances.

4.5.3 Statistical analysis of nearest-neighbor spacings

In the previous section, we concluded that K is a good quantum number for resonances with $K \to K_{max}$ and $K \to K_{min}$, but not for resonances with $K \to 0$. In addition, we found that N and n' are good quantum numbers only for resonances with $K \to K_{min}$. In this section, we shall employ statistical tools for the analysis of NNSs between resonances, linewidths, and Fano q parameters of resonances in order to further confirm these findings.

The integrated NNS distributions from a global analysis of resonances below the different SITs up to the SIT I_{16}, together with Wigner and Poisson distributions, are plotted in Fig. 4.23. For a clearer presentation, only curves for $N = even$ are plotted. Note that the thresholds with $N = odd$ exhibit the same distribution. In this context, "global" means that all resonances below a given ionization threshold, I_N, are taken into account without any restrictions for K. For example, the dotted line marked with $N = 10$ in the text of the figure is extracted from the NNSs between all resonances below the SIT I_{10}. In order to avoid misleading results from possibly missing resonances caused in the region close to each SIT, I_N, or in the beginning of each threshold, which can be caused by convergent problems in the calculations, only the resonances in the middle values of the n_{eff} range were considered in the statistical analysis. Below I_{10}, the dotted line was constructed only from resonances with $n_{eff} = 11$ to 20. An additional reason could be that the Rydberg series become more and more regular due to a small number of perturbers in the region extremely close to each SIT. However, the present calculated data cannot yet reach this region, which can be seen in Fig. 4.8 from the data below the I_{10}. All global NNS distributions below the SIT I_{16}, presented in Fig. 4.23, reveal a
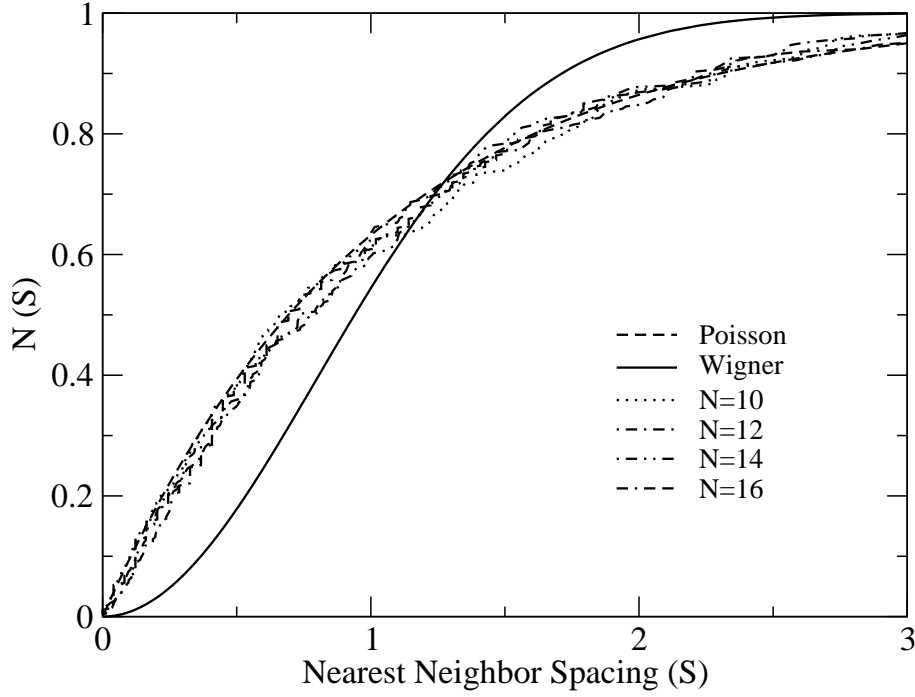
Figure 4.23: Integrated nearest-neighbor spacings (NNS) distributions $N(s)$ for the resonances below the SIT I_{16} using a global analysis. The global NNS distributions $N(s)$ for the resonances below the various SIT I_N are displayed together with a Wigner and a Poisson distribution representing a chaotic and a regular system, respectively.

Poisson form, which indicates that there are still independent subsystems, which can be classified by quantum numbers. From the discussion in the previous section, we know that K and N do not break down completely; there are some regions where they work quite well. In this case, the resonances can be considered to constitute several Rydberg series that are uncorrelated and may be distinguished by different quantum numbers K. Note that although K is mixed for the resonances with $K \rightarrow 0$, all of them can be regarded as one special "Rydberg series" equal to the one with a good K value. In summary, independent and uncorrelated Rydberg series constitute a "regular" system, whose the NNS distribution has a Poisson form. These independent and uncorrelated Rydberg series can be regular or chaotic [10]. In this way, the highest probability $P(S)$ for the NNSs of resonant energy levels occurs at $S = 0$, and then global NNS distributions exhibit a Poisson from (for details, see Sect. 4.2). In previous experimental and theoretical studies for the TCSs, Püttner *et al.* found a transition towards quantum chaos below the SIT I_9 [18]. The Poisson form of the NNSs up to I_{16} in the present study indicates that the transition region from integrability to chaos is much larger, since the quantum number K seem to dissolve rather slowly. Full chaos in $^1P^o$ doubly excited helium may appear at the double-ionization threshold. The trend approaching chaos is analogous to the situation in $^1S^e$ doubly excited helium [19].

The integrated individual NNS distributions for the resonances with $K \rightarrow K_{max}$ below the SIT I_{16} are given in Fig. 4.24. In addition, the curve for the regular Rydberg series
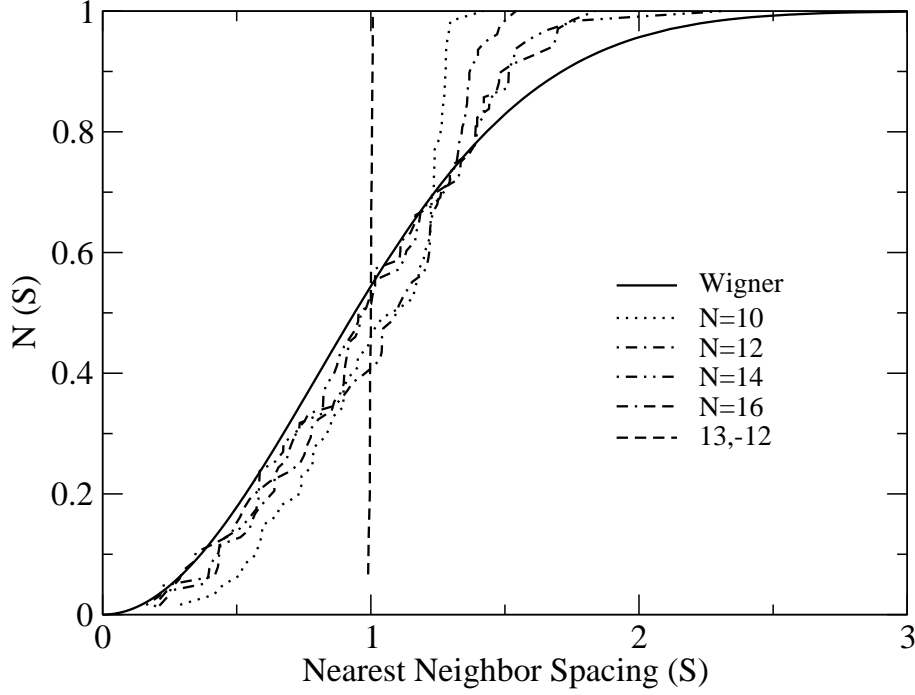
Figure 4.24: Integrated nearest-neighbor spacings (NNS) distributions for the resonances $K \to K_{max}$ below the SIT I_{16} using an individual analysis. The individual NNS distributions obtained for the resonances below the various SIT I_N, classified by good quantum numbers K, are shown together with a Wigner distribution representing a chaotic system. For comparison, the integrated NNS distribution for the regular Rydberg series $13, -12_{n'}$ is also shown.

$13, -12_{n'}$ is also displayed in this figure. In this context, "individual" means that the NNS distributions were obtained from the resonances below a given ionization threshold I_N that belong to a Rydberg series $N, K_{n'}$ with well-defined N and K. In a first step, the NNS distribution is obtained individually for each Rydberg series with well-defined K in the region of $K \to K_{max}$. In order to improve the statistics, the results obtained for the different Rydberg series are added, which results in the plots given in Fig. 4.24. For comparison, the NNS distribution for the regular Rydberg series $13, -12_{n'}$ is also given, which shows a perfect step function. The NNS distributions for the individual analysis of the Rydberg series with K close to K_{max} below the SITs I_{10} to the I_{16} exhibit a form between a step function and a Wigner function. Moreover, the NNS distributions approach a Wigner-like form with increasing ionization threshold I_N, which indicates that the radial quantum numbers N and n' dissolve completely in this region and lose their physics meanings. Since one K-selected Rydberg series, i.e. with the angle between the two electrons and nucleus fixed, can be considered to be a "1-D" case in 3-D helium, a Wigner-like form of K-selected NNS distributions for Rydberg series with $K \to K_{max}$ values is a quantum signature of chaos for the "1-D" case in real 3-D helium. These "1-D" cases in 3-D helium agree very well with those obtained from 1-D helium presented by Püttner *et al.* [18] and confirm their predictions that full Wigner distribution will be found around I_{17}.

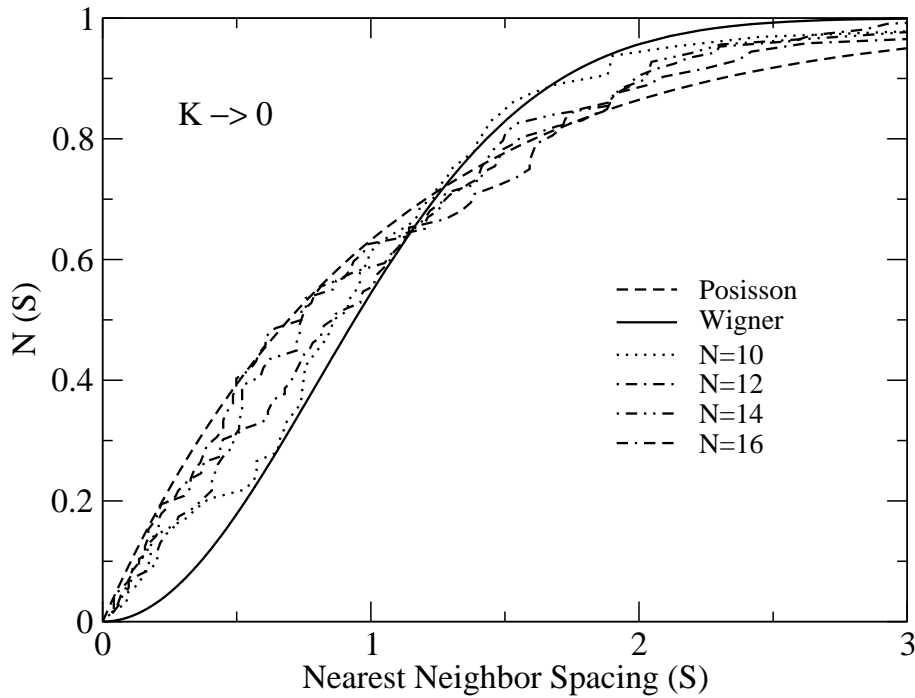In the region for $K \to 0$, Rydberg series with well-defined K values cannot be iden-

Figure 4.25: Integrated nearest-neighbor spacings (NNS) distributions $N(s)$ for the resonances $K \to 0$ below various thresholds up to the SIT I_{16}. The NNS distributions $N(s)$ for the resonances with $-4 < K < 2$ below a given SIT I_N are displayed together with a Wigner distribution and a Poisson distribution representing a chaotic and a regular system, respectively.

tified (see Figs. 4.16 to 4.20). Therefore, one would expect that a perfect Wigner distribution should be found in a statistical NNS analysis. Fig. 4.25 presents the NNS distributions for the resonances in the region of $K \to 0$ ($-4 < K < 2$) below the various SITs up to the SIT I_{16}. The NNS distribution for resonances below I_{10} is in quite good agreement with the Wigner form. Interestingly, the NNS distributions of resonances below higher ionization thresholds match a Poisson form quite well, see e.g. the curve obtained for the region below I_{16}. This is not understood at present.

In very recent calculations by Le *et. al.* [19], statistical studies of the NNSs for $^1S^e$ doubly excited states were performed up to the SIT I_{19}, and the rate approaching a Wigner distribution was found to be slow, in agreement with the present situation for $^1P^o$ doubly excited states; this means that the transition region from integrability to chaos is much broader than previously expected.

4.5.4 Porter Thomas distribution of linewidths

The wave function of discrete states describing the doubly excited resonances can be regarded as representing the eigenvector in a Gaussian orthogonal ensemble (GOE), i.e. it can be described as the random element of matrices. Each eigenvector is of unit norm, and the statistical properties for the components of the eigenvector display a Porter-Thomas distribution [64, 82]. Since the widths Γ of the resonances are related to the eigenvector by Eq. (3.4), one has to assume that the probability $N(x)$ for width Γ exhibits
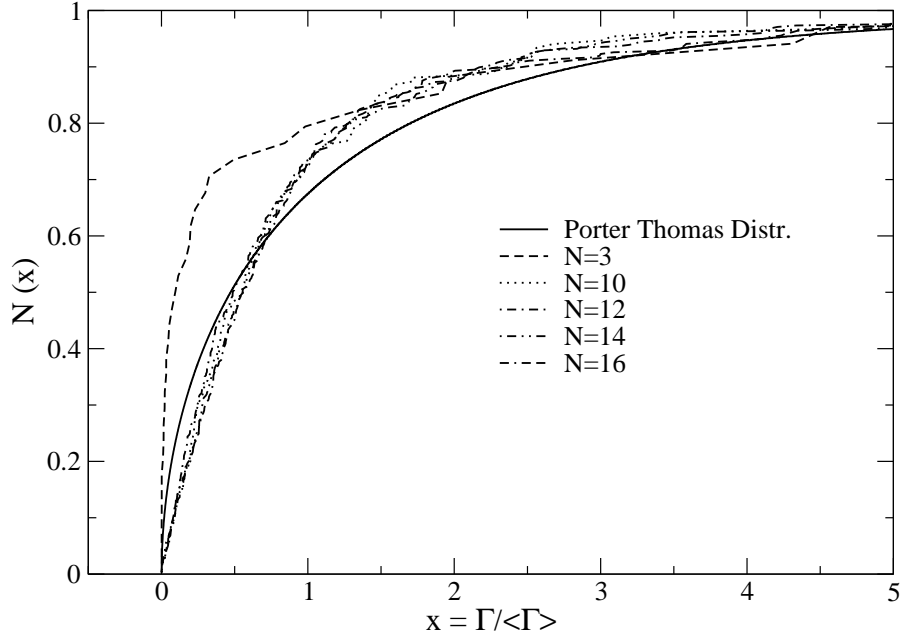
Figure 4.26: Statistical distributions $N(x)$ of resonant linewidths as a function of reduced width in the region below the SIT I_{16}. An integrated Porter-Thomas distribution, representing a chaotic system, is also plotted (solid line).

also a Porter-Thomas distribution [64, 82, 83] given by

$$P(x) = \frac{1}{\sqrt{2\pi x}} exp(-x/2), \tag{4.13}$$

where $x = \Gamma/\langle \Gamma \rangle$ is the reduced linewidth. One can easily see that the smallest widths have the highest probability. This means that the strong statistical fluctuations in the random matrix tend to compensate each other, and the most probable value of a matrix element is zero. In order to improve statistics, we analyze the integrated form $N(x) = \int_0^x dx' P(x')$.

In Fig. 4.26, the statistical probability for the linewidth as a function of reduced width is displayed for the regions below the SITs I_3 and I_{10} up to I_{16}, together with the Porter-Thomas distribution that is plotted as a solid line. The shape of the distributions above I_{10} are almost identical and exhibit a fair agreement with the Porter-Thomas curve. Note that—for a clearer presentation—these statistical distributions are given only for thresholds I_N with $N = even$; the curves for $N = odd$ would show very similar shapes. The $N = 3$ region is regular, with five regular Rydberg series and no perturbers. The statistical probability distribution of the linewidths for the $N = 3$ region is quite different from the results below higher SITs. Interestingly, the eigenvector statistics for a kicked top under conditions that leads to a regular motion in the classical limit, which was presented in Fig. 4.3 of Ref. [65] shows a similar shape as the results for the $N = 3$ region of doubly excited helium given in Fig. 4.26. The lithium atom in a magnetic field was studied in Ref. [83], and the statistical properties of the observed linewidths were also well described by random matrix theory. So far, there are only rather limited data available for statistical studies of linewidths.

4.5.5 Lorentzian distribution of Fano q parameters

So far, we have focused on the statistics of level spacings and linewidths. A distribution of Fano q parameters in a chaotic system had been first derived by W. Ihra in 2002 [84]. According to Ihra's studies, the distribution of Fano q parameters can be derived under two prerequisites: First, the classical motion of high double-excitation resonances has to be chaotic. This ensures that the eigenstates of double-excitation resonances can be described by matrices taken from a Gaussian orthogonal ensemble in random matrix theory [84]. The statistical properties of the Fano q parameter are assumed to be determined by that of the eigenstates. Second, the excitation process and the coupling between a discrete state and final continuum states are assumed to be separated. Therefore, $x \equiv \langle \nu \mid r \mid i \rangle / \langle f \mid r \mid i \rangle$ and $y \equiv \pi \langle \nu \mid V \mid f \rangle$ can be taken as statistically independent random variables [84], where $q = x/y$ given in Eq. (3.5) and i, ν, and f are initial state, discrete state, and final continuum state, respectively. r represents the dipole operator, and the Coulomb operator V controls the autoionization process. The probability distribution for q is given by a Lorentz distribution [84]

$$P(q; w) = \frac{1}{\pi} \frac{w}{w^2 + (q - \overline{q})^2}, \tag{4.14}$$

where $w \equiv \sigma_x/\sigma_y$ is the width of the probability related to the coupling strength V between the discrete states and the continuum states as well as the ratio of the dipole transition matrix to the discrete state and the final continuum states. $\sigma_x(\sigma_y)$ are the variances of the variables $x(y)$. For a strong coupling to the continuum state, i.e. for σ_y being large, the Lorentzian distribution has a small width centered around $\overline{q}$. The same holds if direct photoexcitation dominates over the indirect process because of small σ_x. Of course, in most cases the change of w depends on the competition between direct
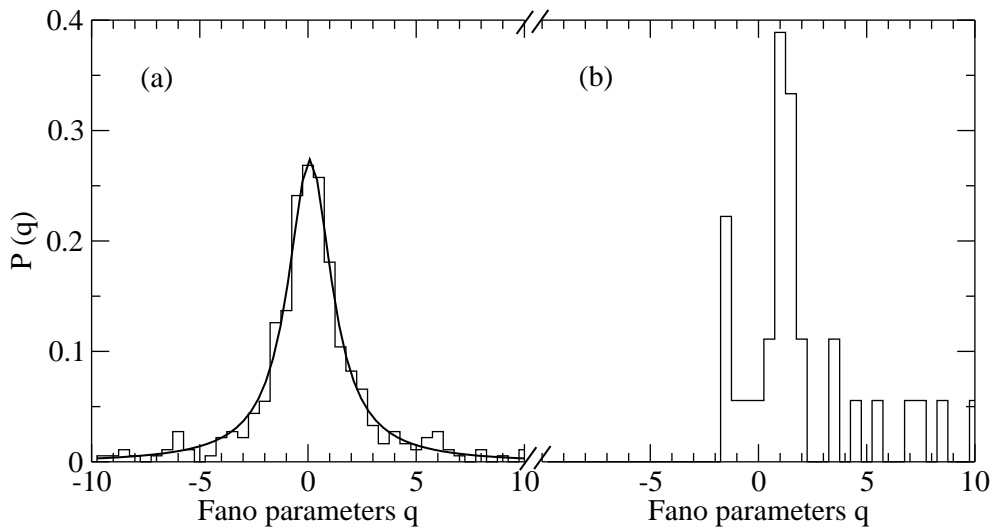

Figure 4.27: Statistical distributions of Fano q parameters (a) below I_{14} and (b) below the SIT I_3. The statistical distribution of q below the SIT I_{14} is fitted by a Lorentzian function plotted as a solid line.

photoexcitation and indirect photoexcitation paths because normally the variations in both decays follow the same direction.

Table 4.1: Widths w and average value $\overline{q}$ extracted from Lorentzian fits to the distributions of Fano q parameters for the various SITs up to I_{17}. The values for the Fano q parameter were taken from the results of the complex-rotation calculations [27].

SITs	w	$\overline{q}$
I_9	2.7	-0.28
I_{10}	2.1	-0.02
I_{11}	2.3	-0.09
I_{12}	2.7	0.10
I_{13}	2.2	0.03
I_{14}	2.5	0.09
I_{15}	2.2	-0.07
I_{16}	2.0	0.15
I_{17}	2.1	-0.05

Statistical distributions of Fano q parameters up to the SIT I_{17} were performed; the results obtained for the SIT I_{14} are shown in Fig. 4.27(a), as an example. The distribution of q below the SIT I_{14} can be described quite well by a Lorentzian function, with $\overline{q}$ close to 0, as predicted by W. Ihra [84]. The distributions in the region between I_9 and I_{17} also match quite well a Lorentzian distribution, with $\overline{q}$ close to 0. In contrast to the distribution of q in the regions of high doubly excited helium, the distribution of q below the SIT I_3 is plotted in Fig. 4.27(b). This statistical distribution is dominated by three peaks around q values of -1.5, 1.0, and 1.5, which correspond to the three regular Rydberg series $3, -2_{n'}$, $3, 0_{n'}$, and $3, 1_{n'}$, respectively. Normally, all members of a regular Rydberg series have similar values of q and, therefore, their distributions do not match a Lorentzian form. The widths w of the statistical distribution for all regions below I_9 to I_{17} are obtained from the fits, and they are summarized in Tab. 4.1. Due to increasing coupling strength to continuum states, w slowly decreases with increasing ionization threshold. These spectra are predicted by Eq. (4.14), while the corresponding classical system is chaotic. To our knowledge, this is the first confirmation of this prediction, and further detailed studies have to be done in the near future.

4.6 The angular correlation mechanism around the double-ionization threshold

The study of electron correlation in the photon-induced double-ionization process of helium has been a topic of considerable interest in the last couple of decades [85−101].

In particular in the vicinity of the double ionization threshold (DIT), it is expected that the double-ionization process is related to a single-ionization process enhanced by the doubly excited states. In 1999, Qiu and Burgdörfer [97] extended the group-theoretical approach for a classification of doubly excited states below the DIT, discussed in Sect. 3.2, to two-electron continuum states above this threshold. This extension allows an extrapolation of angular correlation properties of doubly excited states beyond the DIT, with the result that they can be used to describe doubly ionized states. The propensity rules for the $A = +1$ or -1 symmetries, known for doubly excited resonances, were also found to be suited to perfectly describe the near-threshold behavior of the photon-induced double-ionization process [94]; an interpretation of the quantum number A has been given in Sect. 3.2.2. In this dissertation, we shall show how the angular correlation behavior of doubly excited states below the DIT is extrapolated to doubly ionized states beyond the DIT. Here, we first discuss the triple differential cross section (TDCS) patterns for the double ionization process, from which the angular correlation patterns can be derived.

For linearly polarized light, Huetz *et al.* [90] first established the TDCSs as

$$d\sigma(E_1, E_2, \theta_{12}) = |a_+(E_1, E_2)(cos\theta_1 + cos\theta_2) + a_-(E_2, E_1)(cos\theta_1 - cos\theta_2)|^2, \quad (4.15)$$

where θ_{12} is the angle between the two outgoing electrons. The angles θ_i ($i = 1$ and 2) are the angles of the two electrons with respect to the polarization vector of the light and $E_{1,2}$ are their respective kinetic energies. The amplitudes a_+ and a_- describe transitions to states with $A = +1$ and -1, respectively. Note that quantum number A corresponds to the symmetry of the wave function for doubly excited states under the exchange $r_1 \leftrightarrow r_2$, and that it has the same value as for doubly ionized states under the equivalent exchange $E_1 \leftrightarrow E_2$ [98]. Here, $r_{1,2}$ represent the absolute values of the distances between the two electrons and the nucleus. For equal energy sharing, i.e. $E_1 = E_2 = E_{ex}/2$, it has been observed [92, 93, 96, 99] that the second amplitude in Eq. (4.15) vanishes if one approaches the DIT , in agreement with the Wannier law [85, 87, 91]. Therefore, for equal energy sharing the TDCSs, given in Eq. (4.15), are written as

$$d\sigma(E_{ex}, \theta_{12}) = C_{E_{ex}}(\theta_{12})(cos\theta_1 + cos\theta_2)^2. \quad (4.16)$$

The correlation factor,

$$C_{E_{ex}} \propto exp(-4ln2(\theta_{12} - 180^0)^2/\theta_{FWHM}^2), \quad \text{with } \theta_{FWHM} = \theta_0 E_{ex}^{1/4}, \quad (4.17)$$

has a Gaussian distribution with a width θ_{FWHM} that is related to the excess energy, E_{ex}. The value of the scaled width parameter, θ_0, obtained by different authors, varies from $\theta_0 = 103$ deg $(eV)^{-1/4}$ [86] to 66.7 deg $(eV)^{-1/4}$ [88]. Equation (4.16) for the case of equal energy sharing can also used as a good approximation for unequal energy sharing if $E_{ex} \to 0$ [98]; this has been confirmed by experimental data [90, 92, 93, 96, 99]. It implies that in this region the amplitude a_- in Eq. (4.15) is much smaller than a_+, and in addition, a_+ is insensitive to E_1/E_2, i.e. $a_+(E_1 = E_2) \cong a_+(E_1 \neq E_2)$. Here, the cases of equal energy sharing ($E_1 = E_2$) and of unequal energy sharing ($E_1 \neq E_2$) of doubly
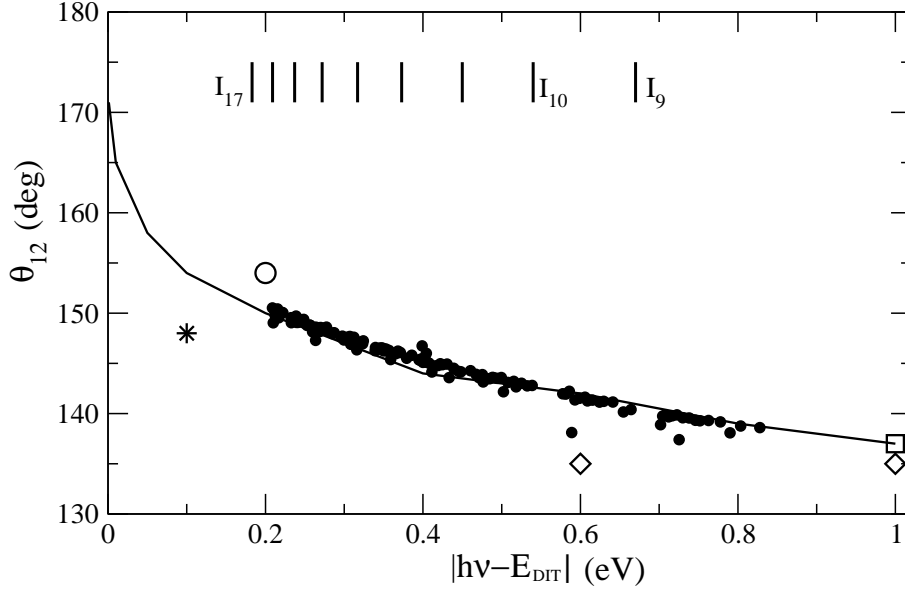
Figure 4.28: Angular correlation parameter, θ_{12}, as a function of energy close to the double-ionization threshold. The filled points represent the calculated doubly excited resonances of the principal Rydberg series $K = N - 2$ from the SITs I_9 to I_{17}; these were indicated in Figs. 4.21 and 4.22 by solid lines. The solid line represents the angular correlation parameter of doubly ionized states taken from Eq. (4.16) by setting $\theta_0 = 80$ deg $(eV)^{-1/4}$. Experimental data for doubly ionized states with $E_{ex} = 2E_1 = 2E_2 = 0.1$, 0.6, and 1.0 eV, respectively, are given by a star [99], an open diamond [93], and an open box [96]; in addition, an open circle represents the result of theoretical calculations by Qiu and Burgdörfer [97]. The positions of single photoionization thresholds, I_N, are marked by vertical bars in the upper part of this figure.

ionized states are equivalent to doubly excited states for two electrons with the same and the different values of the principal quantum numbers N and n', respectively.

In the previous section, we confirmed that the cross section below the DIT is dominated — at least up to the SIT I_{14} — by the principal series $K = N-2$, which corresponds to the classical collinear eZe configuration. Close to the double-ionization threshold, the angle θ_{12} for the principal series $K = N - 2$ increases strongly and reaches 180^0 directly at the DIT (see Fig. 4.22). Therefore, the collinear eZe configuration can be considered to be the most likely one in the vicinity of the DIT. We want to point out that the wave function for the principal series $K = N - 2$ is of $A = +1$ symmetry matching perfectly with the most intense double ionization channels above the DIT, where the amplitude with $A = +1$ symmetry dominates the TDCSs resulting in Eq. (4.16).

In the following, We discuss similarities in the angular correlation properties of the doubly excited states below the DIT and of the doubly ionized states above this threshold. Figure 4.28 displays the energy-dependent angular distribution near the DIT, i.e. the value of θ_{12} as a function of the relative energy, $|h\nu - E_{DIT}|$, for an approach from above and below this threshold. $E_{DIT} \cong 79$ eV is the DIT of helium. The filled points represent the calculated doubly excited resonances of the principal Rydberg series $K = N-2$ from

below the SITs I_9 to I_{17}, which are indicated in Figs. 4.21 and 4.22 by solid lines. The changes of θ_{12} for the principal Rydberg series of the doubly excited states are in good agreement with theoretical values for the doubly ionized states, which is given by the solid curve taken from Eq. (4.16) by setting $\theta_1 = 90^0$ and $\theta_0 = 80$ deg $(\text{eV})^{-1/4}$. The value $\theta_0 = 80$ deg $(\text{eV})^{-1/4}$ agrees with the experimental [93] and theoretical [89] values at $E_{ex} \cong 0.6$ eV. The experimental data for $E_{ex} = 0.1, 0.6,$ and 1.0 eV, respectively, are represented in this figure by a star [99], an open diamond [93], and an open box [96]. The open circle is taken from the theoretical predictions for the doubly ionized states given by Qiu and Burgdörfer [97]. We note from Eq. (4.16) that θ_{12} depends only slightly on θ_1, but shows a strong dependence on E_{ex}. The simulation on the basis of this equation showed that θ_{12} has a maximum value at $\theta_1 = 90^0$ for a constant value of E_{ex}. The experimental TDCSs of Ref. [93] were not measured at $\theta_1 = 90^0$, which have resulted in smaller values of θ_{12} as indicated by the open diamond in Fig. 4.28. In fact, the angular distribution parameter, β, has been confirmed to approach -1 by approaching the DIT from both above [94, 95] and below [102], i.e. the highest probability for the outgoing electrons is at $\theta_1 = 90^0$ with respect to the polarization of light.

In addition, the excess energies, E_{ex}, of the two ionized electrons above the DIT correspond to the binding energies of the doubly excited states below the DIT. Therefore, the doubly excited resonances close to single ionization, i.e. the ones with $n' \gg N$, can be regarded as the counterpart of unequal energy sharing in the double-ionization process. The theoretical results for doubly excited states, presented in Fig. 4.28, show that θ_{12} does not change much below one single ionization threshold. This observation corresponds to the fact that for doubly ionized states close to the DIT θ_{12} is also insensitive to the ratio E_1/E_2 [92, 93]. Considering all these facts, the available experimental results above the DIT and the theoretical results below the DIT are in agreement with those derived from the analytical expression given in Eq. (4.16). Figure 4.28 shows clearly that the angular correlation around the DIT has a mirroring behavior taking the DIT as the mirroring axis. This mirroring angular correlation dynamics around the DIT further improves the understanding to the double-ionization dynamics of helium: the preferential double-ionization path should be the one where the two electrons escape symmetrically and back-to-back. In order to confirm this prediction on the mirroring angular correlation dynamics, more experimental and theoretical work on the TDCSs at $E_{ex} \leq 1$ eV is needed, in particular for $\theta_1 = 90^0$.

Because of the $^1P^o$ symmetry, θ_{12} for the equal-energy-sharing case is not equal to 180^0, even at the DIT, i.e. the TDCSs have a node at $\theta_{12} = 180^0$ on the basis of standard quantum mechanics [98]. As mentioned in Append. A, in the limit of the DIT, the quantum description of helium should lead to a classical mechanical case (Bohr's correspondence principle). This may be considered to be the signature of classical mechanics in the quantum helium system, when E approaches the DIT.